

Unlocking the Potential of Li-Rich Mn-Based Oxides: Surpassing 300 mAh g⁻¹ at Room Temperature in All-Solid-State Batteries

Willy Shun Kai Bong,* Naoya Ishida, Shoko Kitabayashi, Masaki Shimada, Koji Kawamoto, Takuhiro Miyuki, and Minoru Kuzuhara

This study presents a comprehensive assessment of the temperature-dependent electrochemical performance of LiNbO_3 -coated lithium-rich manganese-based oxide (LRMO) cathodes in all-solid-state batteries (ASSBs). The effects of temperature and activation on the performance of LRMO cathodes are systematically investigated through electrochemical characterization and X-ray diffraction and X-ray absorption near-edge structure analyses. LRMO activation significantly improves electronic conductivity by facilitating lithium intercalation within the sulfide-based solid electrolyte (SE). This conductivity enhancement reduces cell resistance more effectively than an elevation in temperature alone. Because of the low conductivity of LRMO at room temperature

($\approx 10^{-6}$ S cm⁻¹), improving the composite cathode's conductivity is critical for reducing cell resistance and enabling LRMO activation. Two strategies are proposed to achieve this: the addition of carbon additives to enhance the electronic conductivity and the application of a LiNbO_3 coating to stabilize the interface between the cathode active material and the SE, thereby minimizing resistance. With these improvements, LiNbO_3 -coated LRMO cathodes with conductive additives achieve a high discharge capacity of over 300 mAh g⁻¹ after 30 cycles at 25 °C. These findings provide valuable insights into optimizing next-generation LRMO-based cathodes and advancing high-performance energy storage systems for ASSBs.

1. Introduction

The growing demands for electric vehicles, including enhanced driving range, safety, and durability, have significantly accelerated the pursuit of all-solid-state batteries (ASSBs).^[1–4] Lithium-rich Mn-based oxides (LRMOs), nanocomposites or solid solutions combining layered LiMO_2 ($M = \text{Ni}, \text{Co}, \text{Mn}$; space group: $\text{R}\bar{3}m$) and Li_2MnO_2 (space group: $C2/m$), are highly promising cathode materials for ASSBs owing to their exceptional energy density, environmental sustainability, and potential to achieve both high capacity and stability.^[5,6] These materials can deliver high specific discharge capacities of 250–300 mAh g⁻¹, enabling energy densities exceeding 1000 Wh kg⁻¹ for LRMO-based cathodes.^[7] However, in conventional liquid electrolyte systems, transition metal (TM) dissolution and severe side reactions at high voltages hinder their practical application.^[7–10] These challenges highlight the need for alternative platforms, such as ASSBs, to fully harness the potential of LRMOs. Moreover, while anionic oxygen redox reactions offer additional charge compensation and capacity benefits, their underlying mechanisms remain poorly understood. However, excessive reliance on oxygen redox reactions can lead

to low initial Coulombic efficiency (CE), capacity fading, and voltage decay, posing further challenges for the long-term performance of LRMO-based systems, which hinders their broad application in conventional liquid ion-lithium batteries.

Recent studies have shown that the dissolution of TMs in liquid electrolytes can be mostly eliminated in ASSBs batteries.^[8–10] The electrochemical performance of LRMOs in ASSBs using various solid electrolytes (SEs), including oxide-,^[11–13] sulfide-,^[10,14–16] and halide-based electrolytes, has been extensively studied.^[17–19] Among these, halide-based SEs have been suggested to be more suitable for LRMOs because of their higher oxidative stability (>4.6 V vs Li/Li⁺) compared to sulfide-based electrolytes,^[19] which exhibit a narrower electrochemical stability window.^[20,21] However, the application of LRMOs in sulfide-based electrolytes remains particularly challenging. To overcome kinetic limitations associated with the Li_2MnO_3 phase and to suppress oxygen evolution during activation—which can degrade the cathode active material (CAM)/SE interface—surface modification strategies, such as LiNbO_3 coatings, are often employed.^[10,14–16,22,23] Despite these efforts, the activation mechanisms of LRMOs in sulfide-based ASSBs remain ambiguous, necessitating a comprehensive study that integrates temperature dependence, coating strategies, and detailed structural and electrochemical analyses.

In light of these complexities, achieving optimal room-temperature performance for LRMO-based cathodes in ASSBs remains a significant challenge.^[24] Insufficient activation of LRMO greatly reduces capacity and cycling efficiency, leading to slower delithiation/lithiation rates and increased internal resistance.^[25–27] Pre-cycling at voltages above 4.5 V (vs Li/Li⁺) has been shown to activate LRMO, resulting in higher specific

W. S. K. Bong, N. Ishida, S. Kitabayashi, M. Shimada, K. Kawamoto, T. Miyuki, M. Kuzuhara
Research Division 3, Department of Commissioned Project
Consortium for Lithium Ion Battery Technology and Evaluation Research Center (LIBTEC)
1-8-31 Midorigaoka, Ikeda, Osaka 563-8577, Japan
E-mail: bong.shunkai@libtec.or.jp

 Supporting information for this article is available on the WWW under https://doi.org/10.1002/batt.202500059

capacities.^[27] However, the exact mechanisms behind this capacity increase, including the electrochemical and structural interactions occurring during activation, are not yet fully understood. Incorporating a LiNbO₃ coating stabilizes LRMO cathodes by reducing side reactions with the SE and maintaining the Mn oxidation state during cycling, which improves performance.^[22] Despite these benefits, the role of LiNbO₃ coatings at different temperatures, particularly in facilitating LRMO activation at room temperature, has not been thoroughly explored. Consequently, the specific effects of LRMO activation, structural stability, and interfacial properties in ASSBs—especially under room-temperature conditions—remain unclear. There is therefore a need for a deeper understanding of these factors to improve the performance of LRMO-based cathodes in ASSBs.

In this study, we explore the temperature-dependent electrochemical performance of LiNbO₃-coated LRMO cathodes with varying LiNbO₃ contents in ASSBs, focusing on improving room-temperature performance. The main objectives are to 1) understand how temperature affects the activation of LRMO and the electrochemical behavior of ASSBs, 2) define the activation process of LRMO and its impact on its crystal structure, and 3) develop strategies to enhance the electrochemical performance of LiNbO₃-coated LRMO cathodes, with an emphasis on increasing capacity at room temperature. The novelty of this work lies in its comprehensive approach, which integrates temperature effects, coating strategies, and detailed structural and electrochemical analyses to gain a deeper understanding of the behavior of LRMO in ASSBs. By examining the influences of these factors on delithiation/lithiation kinetics, phase activation, and structural stability, this study provides valuable insights for optimizing LRMO cathodes for practical energy storage applications.

2. Results and Discussion

2.1. Crystal Structure and Characterization of LiNbO₃ Coating Layer

The LRMO material used in this study was a micrometer-sized, spherical, commercial Li_{1.2}Ni_{0.13}Mn_{0.54}Co_{0.13}O₂ powder supplied by GS Alliance Co., Ltd. The LRMO material was coated with LiNbO₃ at concentrations of 0.2 wt% (LRMO-Nb1), 0.5 wt% (LRMO-Nb2), 1.8 wt% (LRMO-Nb3), and 3.2 wt% (LRMO-Nb4) using a Li–Nb double alkoxide solution, as described in our previous studies.^[28–30] The ASSB cells were assembled in a bulk-type configuration. The composite cathode pellet consisted of LRMO and an argyrodite-type Li_(7-x)PS_(6-x)Cl_x SE ($x \approx 1$, 1.8 g cm⁻³, 2×10^{-3} S cm⁻¹, Mitsui Mining & Smelting); an argyrodite-type Li_(7-x)PS_(6-x)Cl_x SE pellet was used as the separator; and a Li–In alloy foil served as the anode.^[29] The CAMs were manually mixed with argyrodite-type SE in a weight ratio of 7:3 in an agate mortar for 10 min to prepare the composite positive electrode.

Figure 1a presents the powder X-ray diffraction (XRD) pattern and corresponding Rietveld refinement results for the bare Li_{1.2}Ni_{0.13}Mn_{0.54}Co_{0.13}O₂ (LRMO-B) sample. Refined crystal structures were visualized using VESTA.^[31,32] The XRD pattern confirms a layered monoclinic Li₂MnO₃–LiMO₂ structure (M = Ni, Mn, Co;

space group: C2/m) with no detectable impurities. The weaker broader peaks at (020/110) arise from a disordered superlattice associated with Li₂MnO₃ as the end member.^[33,34] Clear splitting of the Kα₁ and Kα₂ peaks indicates high crystallinity. Rietveld refinement yielded a satisfactory fit, verifying the structural integrity and single-phase nature of the LRMO-B sample (Table S1, Supporting Information). To confirm that the crystal structure remains unchanged after the LiNbO₃ coating process, the XRD pattern and Rietveld refinement results of the LRMO-Nb2 sample are shown in Figure 1b and Table S1, Supporting Information. No significant differences were observed, indicating that the coating process does not alter the bulk crystal structure.

To mitigate direct physical contact between the SE and LRMO particles, which could lead to severe side reactions, LiNbO₃ coating layers with varying Nb concentrations were applied to the LRMO particles. The structural and compositional analyses of these coatings were performed using scanning electron microscopy-energy-dispersive X-ray spectroscopy (SEM-EDS), inductively coupled plasma mass spectrometry (ICP-MS), and TEM. Figure 1c shows the SEM images of LRMO-B and the coated samples, revealing that the LRMO particles are submicron-sized (<1 μm). Figure 1d,e shows SEM-EDS elemental mapping results for Nb and the overlapping distribution of Nb and Mn, respectively, indicating a gradual thickening of the coating layer as the Nb concentration increases with the dose of LiNbO₃ in the coating solution. This observation is further quantified by ICP-MS analysis (Figure 1f), which shows a strong linear correlation (R^2 close to 1) between the Nb concentration on the surface and the dose of Nb in the coating solution. Cross-sectional TEM measurements of the LRMO-Nb2 sample confirm the presence of a 5 nm thick LiNbO₃ coating layer (Figure 1g). The amorphous nature of the LiNbO₃ coating is evident from the absence of a crystalline lattice in the TEM images, further confirming that the particles are uniformly covered by an amorphous LiNbO₃ layer.^[30]

The XRD, SEM, and TEM results highlight the structural integrity of the LRMO material and the effective application of amorphous LiNbO₃ coatings. These coatings ensure a controlled thickness, which is essential for mitigating side reactions with the SE.

2.2. Charge–Discharge Performance in the Initial Cycle

The electrochemical performance of LRMO-B, LRMO-Nb1, LRMO-Nb2, LRMO-Nb3, and LRMO-Nb4 as cathodes in an ASSB configuration was evaluated at 25 and 60 °C, using an argyrodite-type SE as the separator and a Li–In alloy as the anode. For the initial capacity test, the cells were charged and discharged for three cycles in a voltage range of 2.0–4.8 V (vs Li/Li⁺) at a constant current (CC) density of 30 μA cm⁻² (C/100). Subsequently, they were held at a constant voltage with a cutoff current of 3 μA cm⁻² (C/1000) at 25 °C. This low current rate was selected to fully utilize the potential of the particles. To investigate the fundamental electrochemical properties of the LRMO material and eliminate the influence of additives, charge–discharge curves were recorded using composite cathodes without conductive carbon or binders.

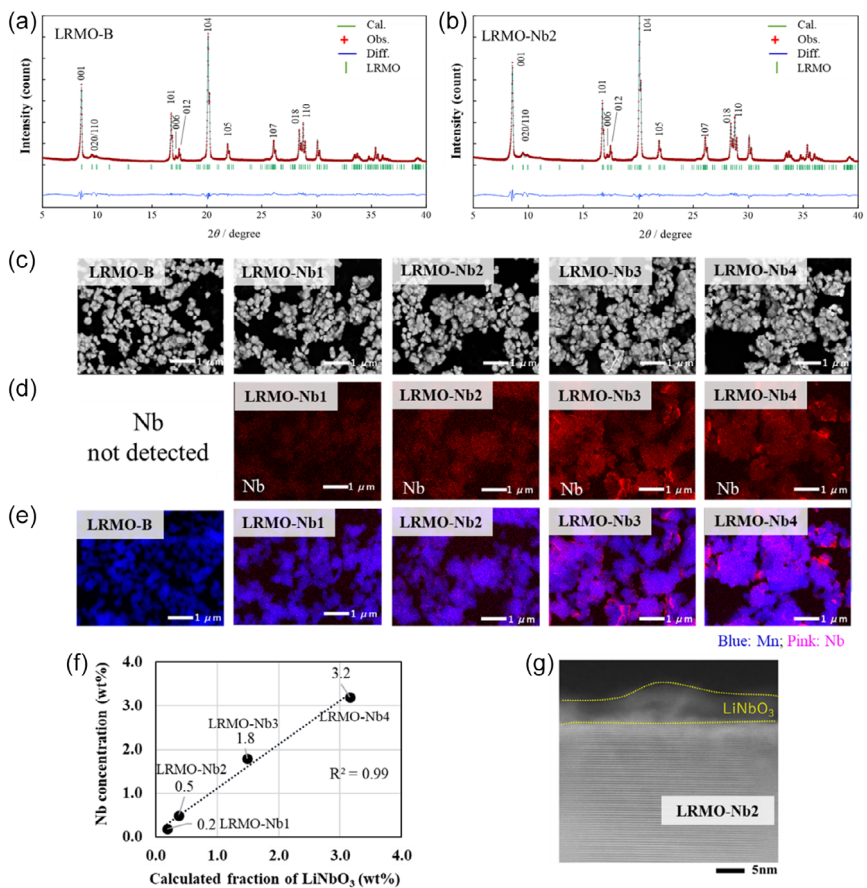


Figure 1. Rietveld fitting results for a) pristine $\text{Li}_{1.2}\text{Ni}_{0.13}\text{Mn}_{0.54}\text{Co}_{0.13}\text{O}_2$ (LRMO-B) and b) LRMO-Nb2. c) SEM images of LRMO-B and LiNbO_3 -coated samples (LRMO-Nb1, LRMO-Nb2, LRMO-Nb3, and LRMO-Nb4). d) SEM-EDX elemental mapping of Nb. e) Overlapping Mn and Nb elemental maps. f) Comparison of the calculated weight fraction of the LiNbO_3 coating and that measured by ICP-MS. g) Cross-sectional high-angle annular dark field-scanning transmission electron microscopy image of LRMO-Nb2, revealing a conformal amorphous LiNbO_3 layer uniformly covering the particle surface.

At 25 °C (Figure 2a), the discharge capacities of the LiNbO_3 -coated LRMO samples (LRMO-Nb1–Nb4) were significantly higher than that of LRMO-B, with LRMO-Nb2 achieving the highest capacity of 200.7 mAh g⁻¹. This improvement is attributed to the LiNbO_3 coating, which enhances the interface stability and suppresses side reactions, thereby improving the overall electrochemical performance.^[28,30,35–37] Despite this, the initial CE remained below 60% for all samples, with LRMO-Nb2 and LRMO-Nb3 showing the highest values of 57.1% and 58.7%, respectively. The lower initial CE of the samples is primarily attributed to irreversible anion redox reactions during the first cycle, leading to oxygen evolution, structural reorganization, and side reactions at the electrode–electrolyte interface.^[23] Specifically, the initial charge capacities observed in LRMO-B and LRMO-Nb1—particularly at the 4.5 V plateau—are significantly lower than the values typically reported for conventional lithium-rich materials, which often exceed 300 mAh g⁻¹.^[7] This discrepancy can be attributed to several factors. First, the ASSB configuration used in this study inherently exhibits kinetic limitations at room temperature, which can hinder the activation of the high-voltage plateau associated with oxygen redox reactions. Full activation of this region generally requires elevated temperatures or extended voltage holds. Furthermore, to investigate the intrinsic

electrochemical behavior of the LRMO material and eliminate the influence of conductive additives, the composite cathodes were fabricated without conductive carbon. While this approach allows for a clearer understanding of the fundamental material properties, it also leads to reduced electronic conductivity and increased interfacial resistance, ultimately limiting capacity.^[26] In addition, incomplete activation of the Li_2MnO_3 component—primarily responsible for the high-voltage plateau—may further contribute to the suppressed capacity due to insufficient electronic pathways and sluggish lithium-ion diffusion in the solid-state environment.

At 60 °C (Figure 2b), all samples exhibited substantially improved discharge capacities and CEs compared to those at 25 °C, with LRMO-B showing a 1.9-fold increase in its discharge capacity. The LiNbO_3 -coated samples had a more moderate increase in their discharge capacities (1.4–1.8-fold), with CEs ranging from 70% to 77%. These substantial increase in the charging capacity, particularly for LRMO-Nb2 and LRMO-Nb3 (approaching 400 mAh g⁻¹), can be attributed to two distinct effects: the LiNbO_3 coating stabilizing the CAM/SE interface and the enhancement of the electrochemical properties of LRMO and the SE at elevated temperatures.^[24,30,35–37] Together, these effects contribute to improved electrochemical performance.

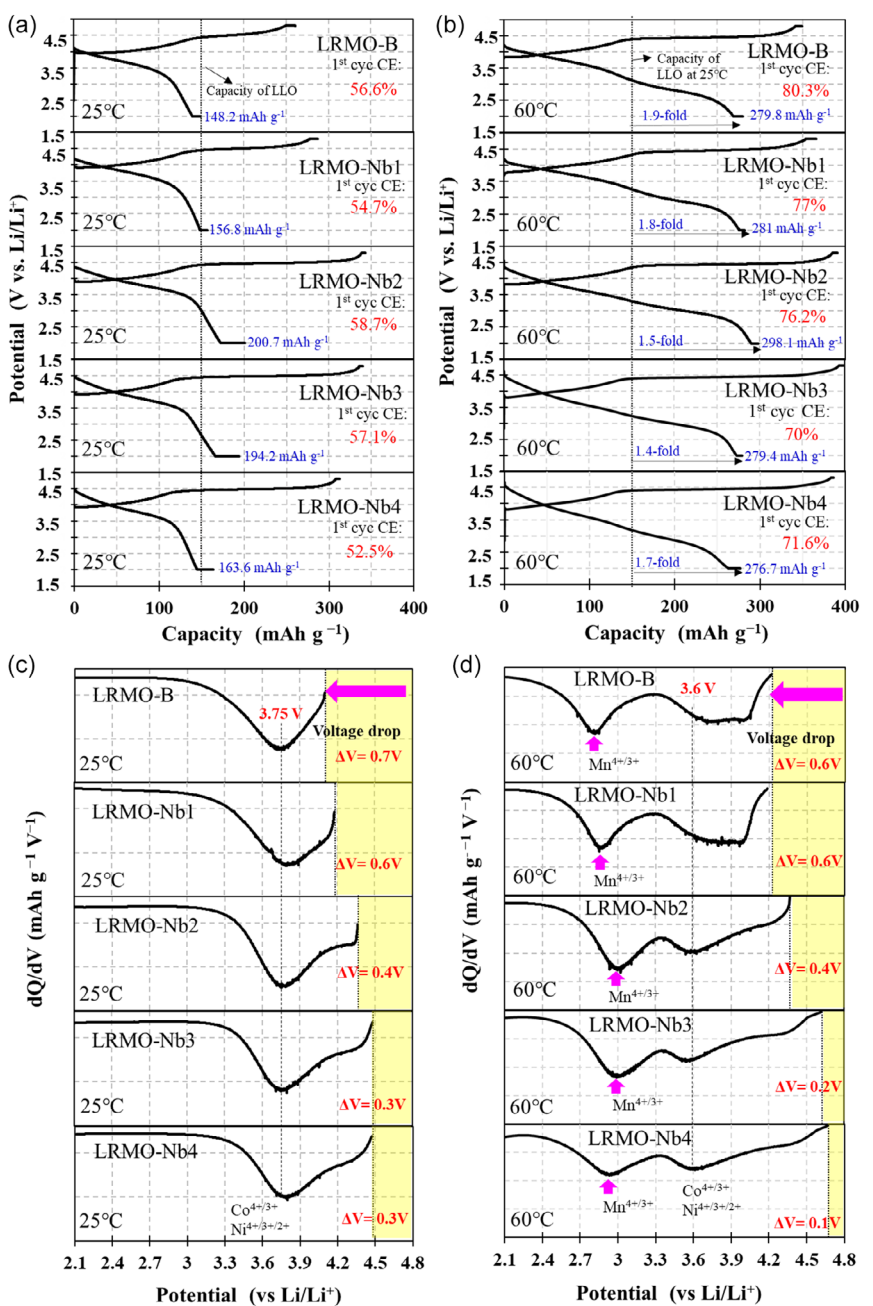


Figure 2. Initial charge-discharge curves for LRMO-B and Nb-coated LRMO samples (LRMO-Nb1, LRMO-Nb2, LRMO-Nb3, and LRMO-Nb4) measured at a) 25 and b) 60 °C, with the initial CE indicated for each sample. Corresponding differential capacity discharge plots at c) 25 and d) 60 °C, respectively, highlighting the voltage drop (ΔV) observed during the initial discharge.

Figure 2c,d shows the differential discharge capacity plots and the voltage drop (ΔV) during the initial discharge, after charging to 4.8 V (vs Li/Li⁺). At 25 °C (Figure 2c), the ΔV value for LRMO-B was the largest (0.7 V vs Li/Li⁺), indicating greater resistance and more significant side reactions during discharging. In contrast, the LiNbO₃-coated samples exhibited smaller ΔV values, with thicker coatings resulting in lower values (0.6, 0.4, 0.3, and 0.3 V vs Li/Li⁺ for LRMO-Nb1–Nb4, respectively). This trend reflects the ability of the LiNbO₃ coating to suppress interfacial reactions and reduce cell resistance, contributing to better electrochemical performance. Similar trends were observed at 60 °C (Figure 2d), generally smaller ΔV values across all samples. LRMO-B and

LRMO-Nb1 showed ΔV values of 0.6 V (vs Li/Li⁺), respectively, while the other LiNbO₃-coated samples exhibited even lower ΔV values (0.4, 0.2, and 0.1 V [vs Li/Li⁺] for LRMO-Nb2–Nb4, respectively). These smaller ΔV values at 60 °C indicate further reductions in interfacial resistance, likely due to the enhanced conductivity of the SE at the elevated temperature, which facilitates faster ion movement and more stable electrochemical behavior. The reduction in ΔV values at higher temperatures underscores the importance of elevated temperature in improving the overall performance of ASSBs by reducing interfacial resistance.

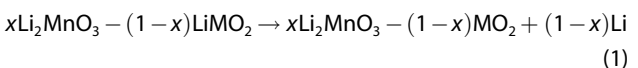
In summary, LRMO-Nb2 and LRMO-Nb3 with 0.4 and 1.5 wt% LiNbO₃, respectively, demonstrated the best performance at

25 °C, offering the highest initial discharge capacities and improved CEs. LRMO-Nb4, with a higher LiNbO₃ content (3 wt%), showed a decrease in its initial discharge capacity, likely due to excessive coating, which increased resistance and led to noticeable performance degradation.^[29] These results highlight the importance of optimizing the thickness of the LiNbO₃ coating for balancing stability and conductivity to achieve better ASSB performance.

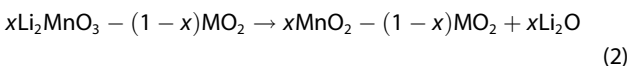
2.3. Redox Dynamics under Varying Voltage and Temperature Conditions

The structure of LRMOs continues to be a subject of active debate; however, these materials exhibit distinct mechanistic behaviors during their charging and discharging processes.^[38–44] The electrochemical reactions that occur during the initial cycles can generally be expressed as follows:^[38–42]

1) Charging (<4.5 V vs Li/Li⁺)



2) Charging (>4.5 V vs Li/Li⁺)



3) Discharging (\approx 2.0 V vs Li/Li⁺)



Electrochemical activation of $x\text{Li}_2\text{MnO}_3 - (1-x)\text{LiMO}_2$ electrodes enhances manganese involvement in the oxidation and reduction reactions during both the charging and discharging processes. During the initial charging process, lithium is extracted from the LiMO₂ component at potentials below \approx 4.5 V (vs Li/Li⁺), until the $x\text{Li}_2\text{MnO}_3 - (1-x)\text{LiMO}_2$ tie-line is reached. At potentials above 4.5 V (vs Li/Li⁺), the Li₂MnO₃ component undergoes an anion redox process, involving the removal of both lithium and oxygen (Equation (1)).^[42] At the end of the charging process (4.8 V vs Li/Li⁺), a metastable MnO₂ phase typically forms, with Mn⁴⁺ as the highest oxidation state (Equation (2)). During the discharging process, lithium ions intercalate into both the LiMnO₂ and LiMO₂ (M = Ni, Co, and Mn) lattices, reducing Mn⁴⁺ to Mn³⁺ and resulting in the formation of stable layered rock-salt-type LiMnO₂ and LiMO₂ phases (Equation (3)).^[43,44] In this work, the phase activation of LRMO refers to the phase transformation from Li₂MnO₃ to LiMnO₂.

In Figure 2c, the peak at \approx 3.75 V (vs Li/Li⁺) during discharging, after charging to 4.8 V (vs Li/Li⁺), is attributed to the reduction of Co⁴⁺/Co³⁺ and Ni⁴⁺/Ni³⁺/Ni²⁺ in the layered structure. This peak shifts slightly to a lower voltage (from 3.75 to 3.6 V vs Li/Li⁺) at 60 °C, indicating higher electrochemical activity and reduced polarization at elevated temperatures (Figure 2d). In addition, a distinctive Mn⁴⁺/Mn³⁺ redox peak is observed below 3.0 V (vs Li/Li⁺) at 60 °C but is absent at 25 °C. This discrepancy suggests that at lower

temperatures, increased cell resistance—attributable to the limited electronic conductivity of the CAM and the lower ionic conductivity of the SE—may impede the phase activation of LRMO.

To further investigate these findings, the charge-discharge curves for the first to third cycles of LRMO-Nb2 and the corresponding differential capacity curves at 25 and 60 °C are shown in Figure 3. The sample exhibits a significantly higher discharge capacity (greater than 280 mAh g⁻¹) during the first to third cycles at 60 °C compared to that at 25 °C (Figure 3a,c). In addition, the CE of the third cycle at 25 °C is \approx 85%, while that at 60 °C is \approx 96%. Both values show a significant improvement compared to the CE in the initial cycle (58.7% at 25 °C and 76.2% at 60 °C, Figure 2a,b). This implies that the electrochemical performance of the battery improves with cycling, especially at higher temperatures. Based on the redox reactions described in Equation (1)–(3) and the differential capacity curves shown in Figure 3b,d, the electrochemical processes of LRMO can be categorized into three distinct voltage regions; the electrochemical characteristics of each region are described as follows.

2.3.1. Region I (<3.7 V vs Li/Li⁺): Activation of Li₂MnO₃ Phase

In this voltage range, the Mn³⁺/Mn⁴⁺ redox reaction plays a critical role in the phase activation of LRMO. At 60 °C, this reaction is clearly observed during the first cycle discharge process after initial charging to 4.8 V (vs Li/Li⁺, Figure 3d). The peaks become stronger with an increasing number of cycles. The distinct Mn³⁺/Mn⁴⁺ redox peaks in the differential capacity curves indicate effective phase activation after the oxygen anion redox process, which occurs above 4.4 V (vs Li/Li⁺) during the initial charging (Figure 3d). However, these peaks are absent at 25 °C (Figure 3b), suggesting suppressed redox behavior likely due to higher resistance at lower temperatures. As shown in Figure 3a,c, the overvoltage during the first charging cycle is higher at 25 °C (3.9 V vs Li/Li⁺) than at 60 °C (3.8 V vs Li/Li⁺), which indicates that increased resistance at lower temperatures leads to greater overvoltage. More importantly, the reduction in overvoltage between the first and third cycles is more significant at 60 °C (1.2 V vs Li/Li⁺) than at 25 °C (0.7 V vs Li/Li⁺). This reveals how elevated temperatures effectively help reduce overvoltage over multiple cycles, aiding in the phase activation of LRMO and improving overall electrochemical performance.

2.3.2. Region II (3.7–4.4 V vs Li/Li⁺): Ni²⁺/Ni³⁺/Ni⁴⁺ and Co³⁺/Co⁴⁺ Redox Reactions

This region is associated with the electrochemical activity of the LiMO₂ phase, where the Ni²⁺/Ni³⁺/Ni⁴⁺ and Co³⁺/Co⁴⁺ redox reactions occur. The redox peaks for Ni and Co are clearly visible for both 25 and 60 °C, indicating that the LiMO₂ phase is more electrochemically active than the Li₂MnO₃ phase due to its higher conductivity (Figure 3b,d). Because longer charge and discharge plateaus are observed at both 25 and 60 °C, the electrochemical activity in this region exhibits less sensitivity to temperature variations compared with Region I. This decreased sensitivity is likely due to the more stable redox reactions

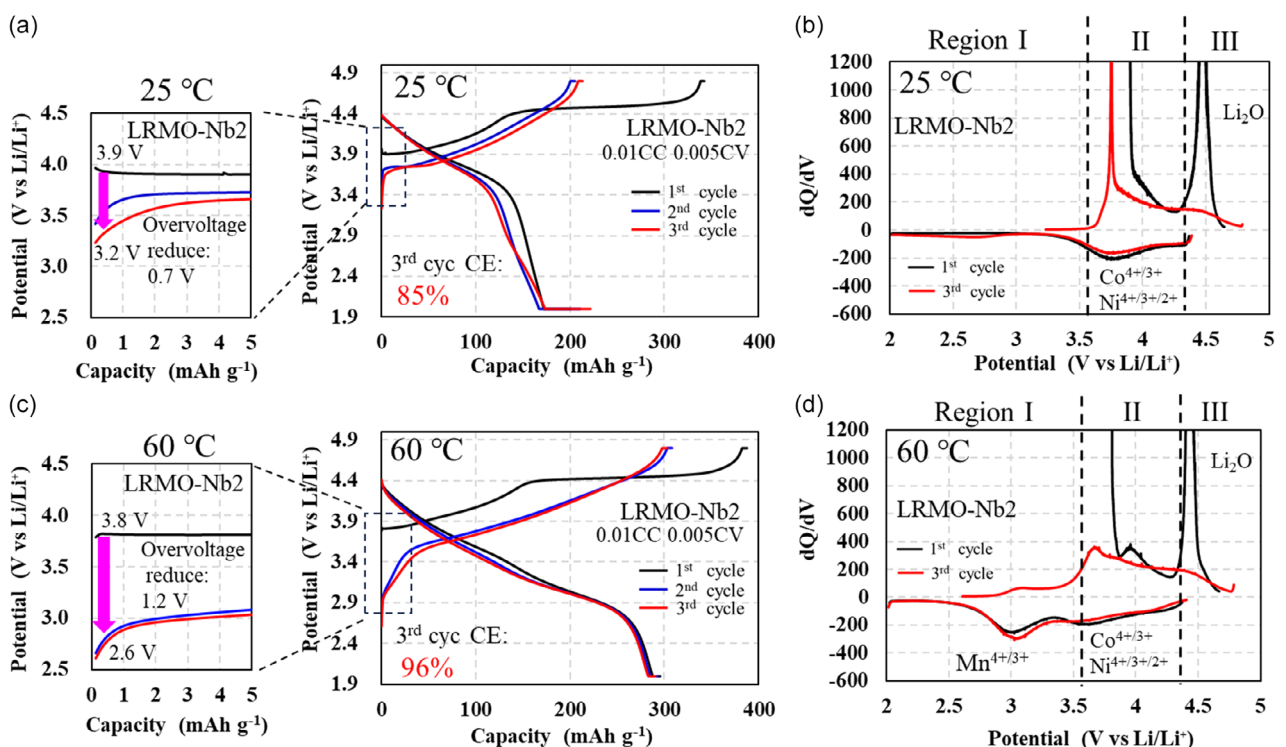


Figure 3. Charge-discharge curves for the first to third cycles of LRMO-Nb2 measured at a) 25 and c) 60 °C. The enlarged views highlight the overvoltage during the first cycle and the voltage drop observed between the first and third cycles. The corresponding differential capacity curves at b) 25 and d) 60 °C. The redox processes identified in the differential capacity curves are categorized into three distinct voltage regions, providing insight into the electrochemical behavior of the material.

occurring in this voltage range that are less influenced by temperature fluctuations. With its higher conductivity, the LiMO₂ phase further minimizes the impact of temperature on electrochemical performance. These observations suggest that the cell resistance in this voltage range may be lower, which in turn reduces polarization.

2.3.3. Region III (>4.4 V vs Li/Li⁺): Oxygen Anion Redox Reaction

At voltages above 4.4 V (vs Li/Li⁺), the oxygen anion redox reaction, i.e., O²⁻ to O₂ⁿ⁻, occurs, involving the partial release of oxygen and lithium from the Li₂MnO₃ phase. This process is critical for activating the Li₂MnO₃ phase, resulting in the formation of Li₂O and other stable products, as well as the transformation of Li₂MnO₃ into MnO₂ during the initial charging process. The reaction is more prominent at 60 °C than at 25 °C, likely due to improved ionic and electronic conductivity, which facilitates the oxygen anion redox process (Figure 3c,d). Conversely, at 25 °C, this reaction becomes less efficient, likely due to increased resistance and reduced conductivity, which decrease charge capacity and limit the electrochemical activity of the Li₂MnO₃ phase (Figure 3a,b).

These findings highlight the critical role of temperature in driving the activation and electrochemical behavior of LRMO-based materials. Elevated temperatures can possibly enhance the conductivity of both the SE and CAM, reducing internal resistance and promoting key redox processes such as the Mn^{3+/4+} reaction and oxygen anion redox activity. Measuring cell

resistance is crucial for understanding these dynamics and accurately assessing the impact of temperature on the electrochemical performance of LRMO-based materials in ASSBs systems.

2.4. Electrochemical Impedance Spectroscopy Analysis

Electrochemical impedance spectroscopy (EIS) was employed to analyze the resistance associated with the different voltage regions in LRMO-B, LRMO-Nb2, and LRMO-Nb4 at 25 °C (Figure 4a) and 60 °C (Figure 4b) during the charging process. Nyquist plots consistently reveal the highest resistance in Region I (<3.7 V vs Li/Li⁺), which is attributed to the Mn^{3+/4+} redox reaction. Region III (>4.4 V vs Li/Li⁺), where oxygen anion redox activity dominates, shows intermediate resistance. Region II (3.7–4.4 V vs Li/Li⁺), associated with Ni^{2+/3+/4+} and Co^{3+/4+} redox reactions, exhibits the lowest resistance due to the higher conductivity and simpler reaction pathways of the LiMO₂ phase. These results highlight the impact of voltage-specific redox processes and phase transformations on resistance. Elevated temperatures notably reduce resistance, especially in Regions I and III, where complex electrochemical activation reactions play a critical role.

The Nyquist plots for all samples measured at 4.0 V (vs Li/Li⁺) at 25 and 60 °C are compared in Figure 4c. At 25 °C, uncoated LRMO-B exhibits the highest resistance (5396 Ω), whereas the LiNbO₃-coated samples LRMO-Nb2 and LRMO-Nb4 show significantly lower resistances of 177 and 179 Ω, respectively. These results highlight the important protective role of the LiNbO₃

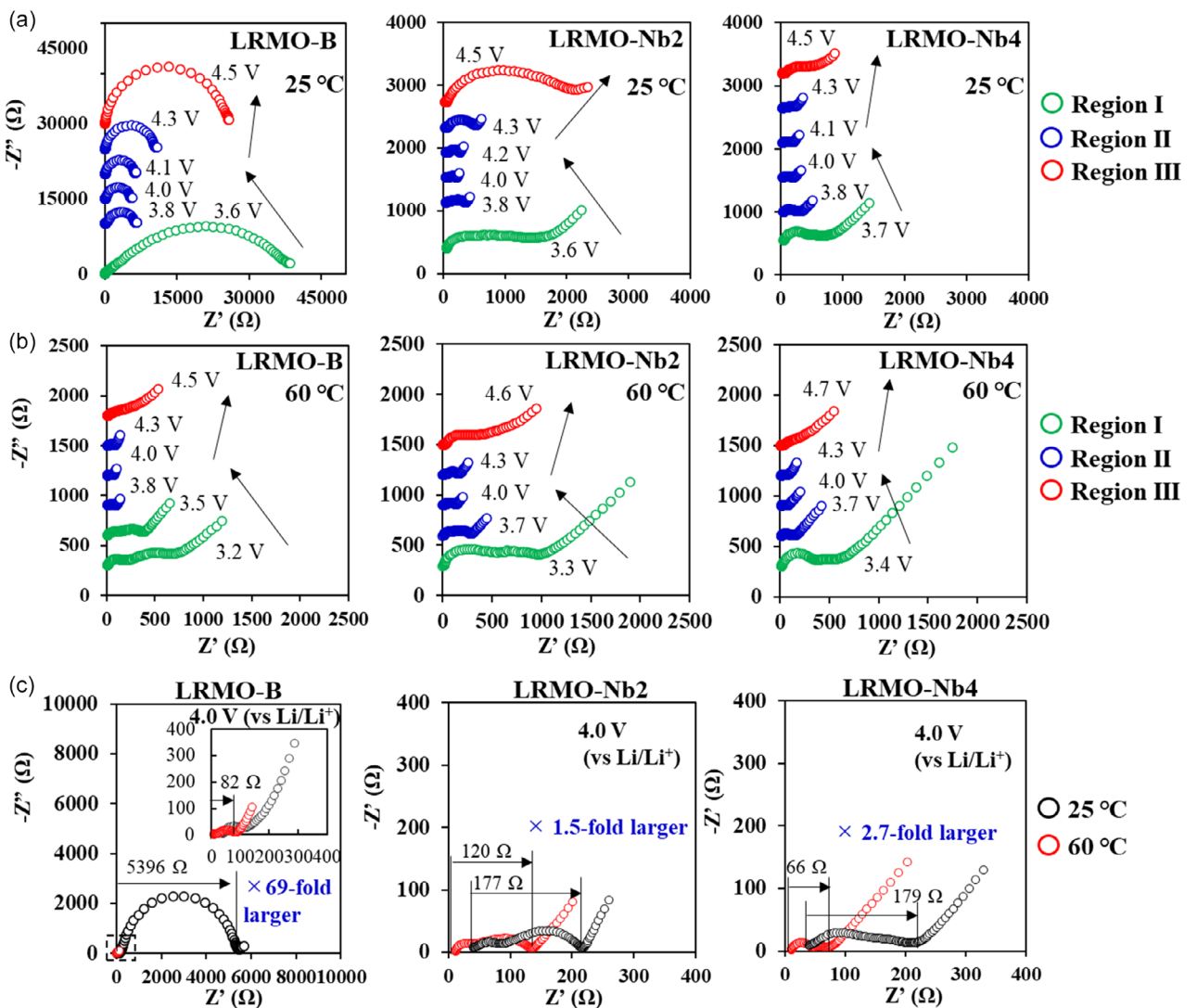


Figure 4. Nyquist plots for voltage regions I, II, and III at a) 25 and b) 60 °C. For comparison, c) the Nyquist plot at 4.0 V (vs Li/Li⁺) for all samples is presented, highlighting differences in resistance across the samples.

coating in mitigating interfacial reactions, thereby reducing resistance. At 60 °C, the resistance of LRMO-B decreases substantially to 82 Ω, while LRMO-Nb2 and LRMO-Nb4 show resistances of 120 and 66 Ω, respectively. The pronounced resistance increase in LRMO-B at lower temperatures can likely be attributed to the reduced ionic and electronic conductivity of LRMO and slower electrochemical kinetics, such as insufficient phase activation or the limited ionic conductivity of the SE at lower temperatures. As the temperature decreases, the lithium-ion mobility and electronic conductivity of both the CAM and SE are hindered, resulting in higher internal resistance. Reduced ion diffusion and impeded charge transfer at lower temperatures significantly degrade electrochemical performance, causing a marked increase in resistance. These findings highlight the stabilizing effects of the LiNbO₃ coating in maintaining low resistance across a wide temperature range.

Overall, our findings underscore the pivotal role of temperature and surface coatings in optimizing the electrochemical performance of LRMO cathodes. Charge-discharge profiles,

dQ/dV analysis, and EIS measurements indicate that elevated temperatures significantly enhance electrochemical performance by promoting the activation of redox processes, particularly the phase activation of LRMO and oxygen anion redox reactions. The LiNbO₃ coating plays a crucial role in stabilizing the electrode–electrolyte interface, effectively reducing resistance and contributing to improved electrochemical performance.

Despite these advancements, the fundamental understanding of the temperature-dependent electrochemical behavior of LRMO cathodes in ASSBs remains inadequate. Specifically, further research is needed to understand how temperature influences the conductivity of LRMO, how electrochemical behavior changes due to phase transitions, and how these factors interact to affect the overall performance. It is crucial to determine which factor—temperature or activation—has a greater influence on the electrochemical performance of LRMO, as well as the specific structural changes that accompany activation. Elucidating these mechanisms is essential for optimizing the design of LiNbO₃-coated LRMO cathodes in ASSBs.

2.5. Decoding the Activation Mechanisms of LRMO Cathodes in ASSBs through Electrochemical Insights

Our charge-discharge profile and EIS analyses suggest that the enhanced performance of LRMO cathodes at elevated temperatures is primarily due to a reduction in cell resistance. We hypothesize that this reduction is influenced by two main factors: 1) the improvement in the electrochemical properties (e.g., conductivity) of both the CAM and SE at higher temperatures and 2) the activation of LRMO. However, the interplay between these factors and their respective impacts on the electrochemical behavior of LRMO remains unclear. We believe that a deeper investigation into the components of the LRMO activation mechanism, and how they are influenced by temperature, will provide crucial insights into optimizing LRMO cathodes for enhanced performance in ASSBs.

To address these questions, we conducted experiments to evaluate the electrochemical properties of LRMO-B, which exhibits the most significant resistance difference between 25 and 60 °C (Figure 4c). These experiments were performed using two types of composite cathodes: one consisting solely of LRMO and the other incorporating LRMO mixed with SE. This comparison allows for an assessment of how the SE influences phase activation, lithium intercalation, and the overall electrochemical performance of LRMO.

Lithium intercalation is required to facilitate the phase activation of LRMO. In this study, we hypothesized that incorporating the SE into the LRMO cathode enhances lithium intercalation owing to the high ionic conductivity of the SE. This approach contrasts with traditional phase activation methods, such as temperature control,^[21] doping,^[5,14] or other modifications,^[25–27] which have been extensively explored. However, the specific role of the SE in facilitating lithium intercalation and phase transformation within the LRMO matrix remains unclear. By incorporating the SE into the composite cathode, we aim to promote the activation of the Li_2MnO_3 phase, thereby providing a novel pathway for efficient phase activation and shedding light on the underlying mechanism of LRMO activation.

To investigate the redox reactions of LRMO-B and gain insight into the underlying mechanism of LRMO activation, cyclic voltammetry (CV) tests were conducted within a voltage range of 2.0–4.8 V (vs Li/Li⁺), both with and without SE. These tests aimed to compare the role of the SE in facilitating lithium intercalation and delithiation, with a specific focus on its impact on phase activation and electrochemical performance. In addition, to evaluate the effect of enhanced conductivity on temperature-dependent performance, the electronic conductivity of LRMO-B particles was

measured at 25 and 60 °C using the Hebb-Wagner polarization technique with a direct current (DC) method.^[45–47] According to Wagner's model, the conductivity of electrons and holes at the reversible side of the LRMO-B | In-Li (anode) interface can be calculated using the following formula:

$$I_{e,h} = RST/FL[\sigma_e(1 - e^{-EF/RT}) + \sigma_h(e^{EF/RT} - 1)] \quad (4)$$

where $I_{e,h}$ represents the absolute value of the electronic current, R denotes the universal gas constant ($8.314 \text{ J mol}^{-1} \text{ K}^{-1}$), S is the cross-sectional area of the sample (m^2), T is the temperature (K), F is Faraday's constant ($96\,485 \text{ C mol}^{-1}$), E is the potential of the cell (V), and L is the thickness of the sample (cm). The σ_e and σ_h terms represent the electronic conductivities (S cm^{-1}) due to electrons and holes, respectively.

For the both electronic conductivity and CV measurements, a composite cathode was prepared by mixing LRMO-B particles with argyrodite-type SE in a weight ratio of 7:3 using an agate mortar. A 100 mg portion of this mixture was then pressed at 588 MPa into a pellet with an area of 1 cm^2 . In-Li alloy was pressed at 98 MPa to form the anode, providing a stable anode potential of 0.62 V (vs Li/Li⁺). This setup allowed for an accurate assessment of the electrochemical properties of the composite cathode, including the role of the SE in enhancing lithium intercalation and the overall electrochemical behavior of the system.

The σ_e and σ_h values before and after the CV tests are summarized in Table 1. Before the CV tests, the electronic conductivity at 25 °C was similar for both the SE-mixed and non-SE-mixed samples ($\approx 1.3 \times 10^{-6} \text{ S cm}^{-1}$). At 60 °C, the conductivity for the SE-mixed samples and non-SE-mixed samples increased to 7.1×10^{-6} and $6.6 \times 10^{-6} \text{ S cm}^{-1}$, respectively. These observations highlight two key points. First, that there were no significant differences in conductivity between the SE-mixed and non-SE-mixed samples before the CV tests at both 25 and 60 °C suggests that lithium intercalation and phase activation did not occur prior to the CV tests, resulting in unchanged conductivity across both temperature conditions. Second, the substantial increase in electronic conductivity (approximately fivefold) for both the SE-mixed and non-SE-mixed samples when the temperature increased from 25 to 60 °C suggests that higher temperatures enhance electron mobility, thereby improving the electronic conductivity of the composite cathode. Notably, the hole conductivity was extremely low for all samples before the CV tests (ranging from $\approx 10^{-54}$ to $\approx 10^{-51} \text{ S cm}^{-1}$), indicating negligible hole conduction, even in the SE-mixed samples.

To further investigate the electrochemical behavior associated with phase activation, we conducted CV tests on SE-mixed

Table 1. The electron and hole conductivity values, σ_e and σ_h , measured before and after CV testing at 25 and 60 °C.

Status	Sample	25 °C	60 °C	25 °C	60 °C
		$\sigma_e [\text{S cm}^{-1}]$	$\sigma_e [\text{S cm}^{-1}]$	$\sigma_h [\text{S cm}^{-1}]$	$\sigma_h [\text{S cm}^{-1}]$
Before CV	LRMO-B without SE	1.3×10^{-6}	6.6×10^{-6}	2.4×10^{-52}	9.8×10^{-52}
	LRMO-B with SE	1.3×10^{-6}	7.1×10^{-6}	5.0×10^{-54}	4.6×10^{-51}
After CV	LRMO-B without SE	1.4×10^{-6}	6.3×10^{-6}	2.2×10^{-52}	9.2×10^{-52}
	LRMO-B with SE	1.0×10^{-5}	7.0×10^{-5}	9.0×10^{-51}	1.3×10^{-49}

and non-SE-mixed LRMO-B cells at 25 and 60 °C. The CV tests were conducted at a scan rate of 1.0 mV s⁻¹ in the voltage range of 2.0–4.8 V (vs Li/Li⁺) for 10 cycles (Figure 5). The non-SE-mixed cell exhibited a linear increase in current with rising voltage but lacked distinct reduction peaks during the reverse scan (Figure 5a), indicating that lithium intercalation and deintercalation did not occur in the absence of SE, despite fast electron transfer. In contrast, the SE-mixed cell exhibited distinct oxidation peaks starting at ≈3.5 V (vs Li/Li⁺) at 25 °C and 3.0 V (vs Li/Li⁺) at 60 °C, with corresponding reduction peaks starting at 4.0 V (vs Li/Li⁺) at 25 °C and 3.5 V (vs Li/Li⁺) at 60 °C (Figure 5b). Notably, at 60 °C, the current at 4.8 V (vs Li/Li⁺) was four times greater than that at 25 °C, reflecting a substantial improvement in ionic and electronic mobility. These observations confirm the reversible delithiation and lithiation processes during CV tests, substantiating the effectiveness of our strategy to promote lithium intercalation through SE addition. This approach successfully facilitates lithium transport, proving its utility in activating the electrochemical processes in LRMO cathodes compared to non-SE-mixed samples.

The second, fifth, and tenth cycles of the SE-mixed cell at 25 and 60 °C are shown in Figure 5c,d, respectively, revealing key trends: the progressive activation of the LiMnO₂ phase at 25 °C and the earlier stabilization of phase activation at 60 °C. The first cycle was excluded because the SE is generally unstable during the initial cycle due to its tendency to undergo decomposition, form interphase layers, and experience structural adjustments, with its oxidation reaction dominating the cell's electrochemical activity. By excluding the first cycle, we were able to focus on the stabilized behavior of the SE and LRMO material,

allowing better insight into their intrinsic electrochemical performance. As shown in Figure 5c, at 25 °C, the areas corresponding to both oxidation and reduction reactions gradually increased with the number of cycles, indicating the progressive activation of the LiMnO₂ phase. At 60 °C, the activation of the LiMnO₂ phase appeared to be completed during the second cycle, as indicated by the stable currents observed in subsequent cycles (Figure 5d). After 10 cycles, the current decreased to 85% of its initial value, likely due to the formation of a degradation layer at the electrode–electrolyte interface. This suggests that the oxidation of the SE is responsible for hindering ion and electron mobility, leading to performance degradation overtime. Notably, the current at 4.8 V (vs Li/Li⁺) during the tenth cycle (around 7 mA) was ≈3.5 times smaller than that at 25 °C (around 2 mA). This indicates that elevated temperatures significantly reduce cell resistance, enhancing ion and electron mobility, which in turn increases the current and improves the electrochemical activity of ASSB cells.

Figure 6 shows the Nyquist plots of LRMO-B, both with and without SE, at 25 and 60 °C, before and after the CV tests. The phases before and after the CV tests are referred to as "before activation" and "after activation," respectively. After activation at 25 °C, the resistance decreased significantly from $265 \times 10^5 \Omega$ (without SE) to 576Ω (with SE), representing a 46 007-fold reduction (Figure 6a,c). Similarly, at 60 °C, the resistance decreased from $5.8 \times 10^5 \Omega$ (without SE) to 175Ω (with SE), corresponding to a 3314-fold reduction (Figure 6d,f). The greater decrease in resistance at 25 °C compared to that at 60 °C can be attributed to the temperature-dependent electrochemical behavior of the LRMO material. At lower temperatures, non-SE-mixed LRMO-B exhibits

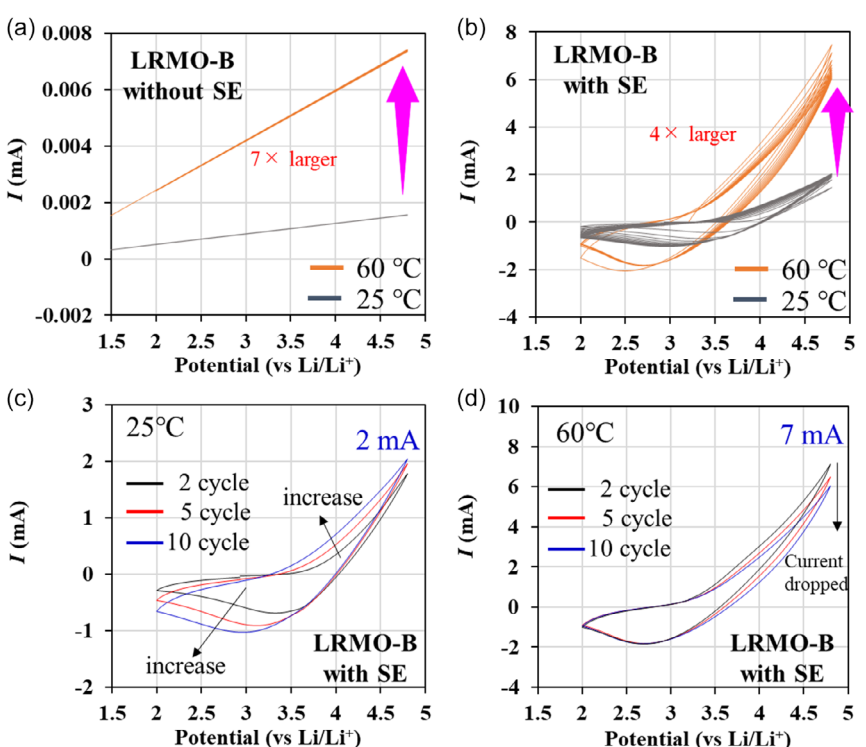


Figure 5. CV curves of LRMO-B a) without and b) with SE for 10 cycles. The 2nd, 5th, and 10th cycles of the SE-mixed cell at c) 25 and d) 60 °C.

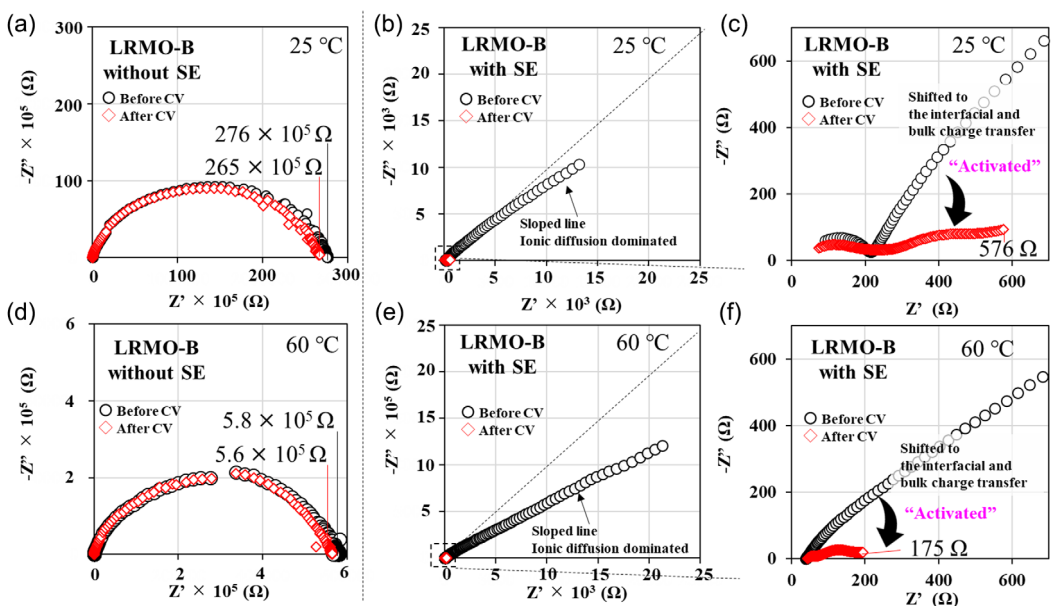


Figure 6. Nyquist plots of LRMO-B with and without SE at a–c) 25 and d–f) 60 °C, recorded before and after CV testing. Enlarged sections of the impedance spectra for SE-mixed LRMO-B cells at c) 25 and d) 60 °C.

significantly lower conductivity, reflected in its higher initial resistances of $276 \times 10^5 \Omega$ and $5.8 \times 10^5 \Omega$ at 25 and 60 °C, respectively. In the SE-mixed LRMO sample, phase activation by the SE has a greater impact on reducing resistance at 25 °C, where the lower initial conductivity of LRMO makes the role of the SE more critical. At 60 °C, the elevated temperature already improves the conductivity of both the SE and LRMO, reducing the additional benefits of SE mixing. Consequently, the reduction in resistance is more significant at 25 °C, where the SE plays a pivotal role in activating the LRMO phase and enhancing overall conductivity. Notably, as shown in Figure 6, we report for the first time that the activation of LRMO is critical for enhancing electronic conductivity during the charge–discharge process. This activation leads to reduced cell resistance and significantly improves the electrochemical performance of ASSBs. These findings highlight the pivotal role of phase activation in boosting electronic conductivity at both 25 and 60 °C, ultimately resulting in substantial performance enhancements in ASSB cells.

The Nyquist plots of the SE-mixed sample before and after CV testing at 25 and 60 °C are presented in Figure 6b,e, respectively. Prior to the CV tests, the Nyquist plot for the SE-mixed sample exhibit a sloped line characteristic of Warburg impedance at both 25 and 60 °C, indicating that ionic diffusion was the primary contributor to resistance. After the CV tests, two distinct semicircles emerged, signifying a transition to interfacial and bulk charge transfer processes. The right semicircle represents interfacial resistance, while the left semicircle corresponds to bulk charge transfer (Figure 6c,f). This transition signifies the activation of the LRMO phase and highlights the critical role of the SE in enhancing charge transfer efficiency. The shift from Warburg impedance to charge transfer processes indicates that, following phase activation, the improved conductivity facilitates more efficient electron flow at the electrode–electrolyte interface and

within the bulk material. These benefits are amplified at elevated temperatures due to enhanced ionic and electronic mobility, which further reduces resistance and improves charge transfer rates. Notably, this is the first demonstration that this enhanced charge transfer plays a pivotal role in reducing cell resistance and significantly improving electrochemical performance, particularly at elevated temperatures.

To investigate the relationship between the impedance changes observed in the Nyquist plots and the electronic conductivity of LRMO, we measured the electronic conductivity of cells with and without SE, both before and after the CV tests, as shown in Figure 7 and Table 1. For the cells without SE, no significant

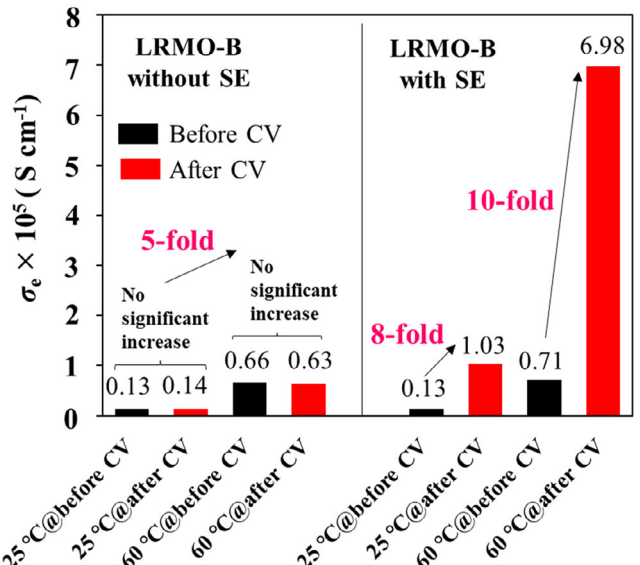


Figure 7. Comparison of electronic conductivity in cells with and without SE, measured before and after CV testing.

increase in conductivity was observed after CV at either 25 or 60 °C, corresponding to negligible changes in cell resistance (Figure 6a,d). In contrast, the SE-mixed cells showed an eightfold to tenfold increase in conductivity after CV compared to before CV at both temperatures. This result indicates that the presence of the SE greatly enhances the electronic conductivity of LRMO cathodes after the CV test, which is accompanied by a shift from Warburg impedance to charge transfer impedance (Figure 6c,f). These findings demonstrate that the SE plays a critical role in activating the LRMO phase and improving its electrochemical performance by enabling more efficient charge transfer processes. The lack of improvement in conductivity for cells without SE confirms that the SE is essential for phase activation and enhanced conductivity. Overall, these results highlight the importance of the SE in increasing charge transfer efficiency, reducing cell resistance, and improving the electrochemical performance of LRMO-based composite cathodes.

In addition, as shown in Table 1, the hole conductivity of SE-mixed cells after the tenth CV cycle at 60 °C increased significantly, from 9.8×10^{-52} to $1.3 \times 10^{-49} \text{ S cm}^{-1}$, representing an increase of approximately two orders of magnitude. This improvement in hole conductivity indicates that oxygen anion redox processes became more active at elevated temperatures. These processes facilitated redox reactions and generated oxygen vacancies, which play critical roles in enhancing electronic conductivity. Our findings support the hypothesis that incorporating the SE improves the delithiation and lithiation kinetics of LRMO, enhancing phase activation and increasing electronic conductivity after cycling.

Figure 8 provides a schematic overview of the relationship between elevated temperature, phase activation, and their

combined effects on conductivity and cell resistance, emphasizing the material's structural-electrochemical interplay. Phase activation in LRMO refers to the process of increasing its electronic conductivity during electrochemical cycling, which significantly reduces cell resistance. At 25 °C, in cells without SE, there was no significant change in conductivity before and after activation, indicating that the LRMO particles remained inactive. However, when the temperature was increased to 60 °C, the electronic conductivity of LRMO increased fivefold, indicating that elevated temperatures enhance electron mobility in the material (Figure 7). For SE-mixed cells, the conductivity increased eightfold at 25 °C and tenfold at 60 °C after the CV test, surpassing the effect of elevated temperature alone (cells without SE, fivefold). This demonstrates that phase activation, facilitated by the SE, has a larger impact on conductivity than temperature elevation alone. While higher temperatures enhance the intrinsic conductivity of LRMO, the SE enables more efficient phase activation, further boosting charge transfer and electronic conductivity. This synergistic improvement significantly enhances the electrochemical performance of LRMO-based cathodes. These findings highlight the importance of optimizing phase activation and electronic conductivity to fully unlock the potential of LRMO in ASSBs.

2.6. Exploring Temperature-Driven Structural Changes in LRMO: A Combined XRD and X-Ray Absorption Near-Edge Structure Approach

To study the structural evolution of LRMO at 25 and 60 °C, XRD and X-ray absorption near-edge structure (XANES) analyses were conducted. XRD revealed changes in the crystal structure, while XANES provided detailed information on Mn oxidation state

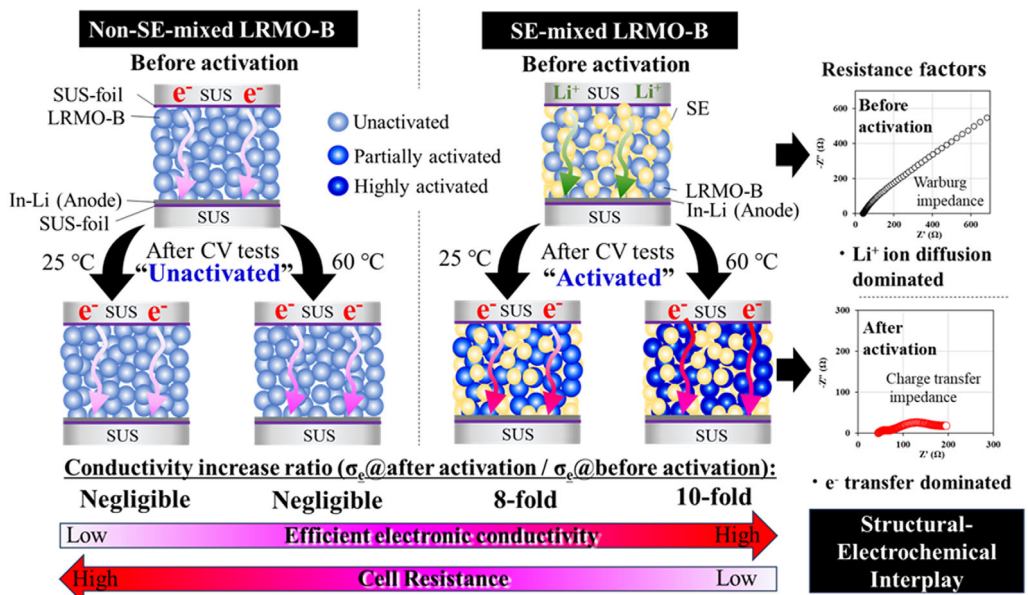


Figure 8. Schematic of LRMO-B without (left) and with SE (right), highlighting the effects of elevated temperature and phase activation on electrochemical properties such as conductivity and resistance. The schematic compares conductivity ratios at 25 and 60 °C, demonstrating that phase activation results in a significant eightfold to tenfold increase in electronic conductivity and a notable reduction in resistance. In contrast, temperature alone has a minimal impact on conductivity or resistance. This highlights the pivotal role of phase activation in improving the performance of LRMO cathodes, particularly at lower temperatures, and underscores the relationship between the structural changes induced by phase activation and electrochemical properties in ASSBs. SUS, stainless steel.

variations. Together, these techniques offered valuable insights into the structural modifications caused by phase activation and their impact on the material's electrochemical performance.

XRD measurements were conducted on LRMO-Nb3 samples after the initial charge and discharge cycles at both 25 and 60 °C. LRMO-Nb3 was chosen due to its superior initial charge capacity, nearly reaching 400 mAh g⁻¹ at 60 °C (Figure 2b), making it ideal for detecting structural modifications. Rietveld analysis provided good fits for both the LRMO-Nb3 and SE phases, as shown in Figure 9a and Table S2, Supporting Information. The XRD patterns confirmed that no by-products were formed during the reaction between LRMO-Nb3 and the SE, and each phase retained its original crystal structure. Interestingly, the lattice parameters of the sample charged at 25 °C, which showed lower capacity (Figure 2a), were smaller compared to those of the sample charged at 60 °C (Table S2, Supporting Information). In addition, the cell volume of the sample charged at 25 °C contracted by 1.6% compared to its pristine state, while the sample charged at 60 °C showed only a 1% contraction. These findings indicate that structural changes in LRMO are more pronounced at lower temperatures, likely due to slower delithiation and lithiation kinetics. These slower kinetic processes increase resistance and reduce capacity (as evident in Figure 3a), potentially leading to incomplete structural adjustments that prevent full lattice shrinkage at higher voltages. Consequently, the LRMO structure remains more expanded at 25 °C. In contrast, at 60 °C, faster kinetics enabled more complete structural changes, including greater shrinkage, which facilitates more efficient ion and electron transport.^[48,49] These observations highlight the temperature-dependent nature of LRMO's structural evolution and its impact on electrochemical performance.

To further investigate these structural changes, Figure 9b summarizes the refined TM occupancies and calculated vacancies

(Vac.) in the TM layer at the 4g and 2b sites in the initial charged and discharged states at 25 and 60 °C. The TM layer vacancy, a measure of the fraction of unoccupied sites in the TM layer, was calculated using the formula:

$$\text{TM layer vacancy} = 2/3 \times (\text{Vac.}4g) + 1/3 \times (\text{Vac.}2b) \quad (5)$$

The TM layer vacancy is unitless because it represents a proportion of the total TM sites.^[33,34] The TM layer vacancy at the 4g sites in the charged state is significantly smaller at 25 °C (0.008) compared to at 60 °C (0.159). This indicates that vacancy formation in the TM layer is more pronounced at higher temperatures, likely due to faster kinetics during charging, which facilitate more extensive vacancy formation. These findings suggest that elevated temperatures enhance phase transitions and improve electrochemical behavior. The TM layer compositions at the charged state are represented as (Mn, Ni, Co)_{0.88}□_{0.12} at 25 °C and (Mn, Ni, Co)_{0.83}□_{0.17} at 60 °C (where □ denotes Vac.), and the refined crystal structures are shown in Figure 9c.

The reduced TM layer vacancy at 25 °C suggests that slower delithiation and lithiation kinetics at this temperature suppress oxygen anion redox reactions and hinder the activation of LRMO during initial charging.^[50] This suppression limits critical processes such as the oxygen anion redox reaction and the LiMnO₂ phase transformation, as depicted in Figure 8, ultimately reducing electrochemical performance. Conversely, at 60 °C, faster kinetics promote the activation of LRMO and oxygen anion redox reactions, leading to greater TM layer vacancy formation and improved electrochemical performance.

After initial discharging, the TM layer vacancies at the 4g sites were 0.196 and 0.186 at 25 and 60 °C, respectively. This indicates that the impact of temperature on vacancy formation is more pronounced during charging, with higher temperatures

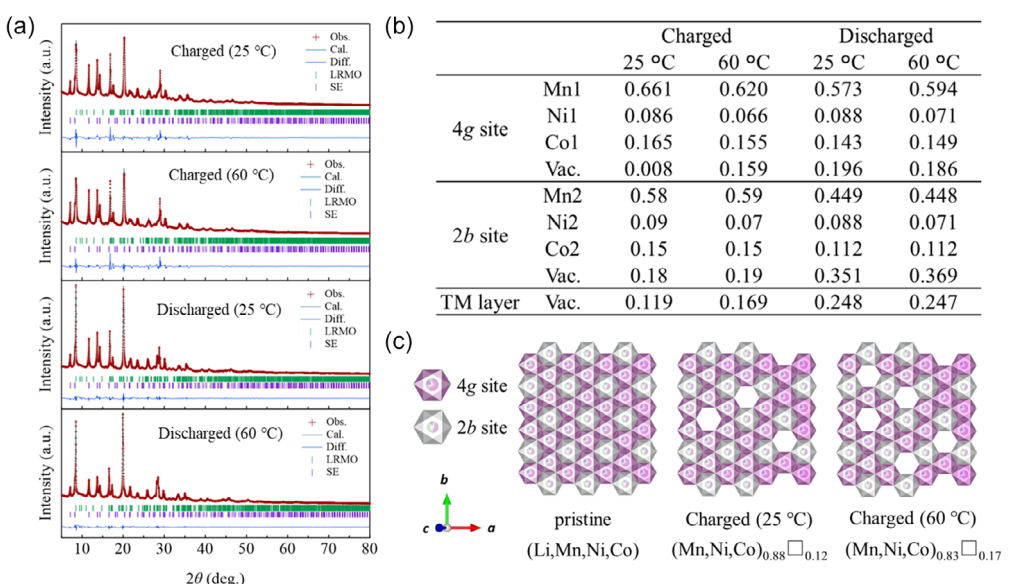


Figure 9. a) Rietveld analysis of LRMO-Nb3 after its initial charge and discharge at 25 and 60 °C; b) refined TM occupancies and vacancies (Vac.) in the TM layer at the 4g and 2b sites in the initial charged and discharged states at 25 and 60 °C; c) refined crystal structure of LRMO-Nb3, illustrating the TM layer vacancies after the initial charge at 25 and 60 °C. The analysis reveals significant changes in the crystal lattice, with a distinct vacancy formation in the TM layer, highlighting the influence of temperature on the structural evolution and TM distribution. □, TM layer vacancy.

facilitating faster kinetics and greater vacancy formation. However, the smaller difference in vacancy levels between 25 and 60 °C after discharge suggests that phase transitions and vacancy formation processes may be partially reversible or stabilized during discharging. These findings demonstrate that the LRMO crystal structure undergoes significant changes during charging, especially under elevated temperatures. Refined TM occupancy analysis revealed that higher temperatures promote greater vacancy formation at the 4g sites during charging, which enhances phase transitions and electrochemical performance. In contrast, lower temperatures result in slower kinetics, suppressing material activation and reducing efficiency. Future operando studies are needed to further elucidate these mechanisms.

To avoid interference from the LiNbO₃ coating, the LRMO-B sample was used to measure Mn oxidation states during charging and discharging using XANES. This ensures that the observed changes reflect the intrinsic properties of the LRMO material, providing a clearer understanding of its redox activities and Mn oxidation states. Mn K-edge XANES spectra for LRMO-B were collected at 4.5 and 4.8 V (vs Li/Li⁺) during initial charging, as well as at 2.0 V (vs Li/Li⁺) after initial discharging. Additional measurements were performed at the fully charged and discharged states during the second cycle. These spectra were compared with reference samples (Mn²⁺O, LiMn³⁺O₂, and Li₂Mn⁴⁺O₃), as shown in Figure 10, to analyze the changes in Mn oxidation states in the LRMO particles. This comparison provides valuable insights into the evolution of Mn oxidation states during charging and

discharging, revealing structural transformations in the Li₂MnO₃ component at various potentials.

Figure 10a–c shows that during charging at 60 °C, the Mn K-edge peak shifted from 6558 eV at 4.5 V (vs Li/Li⁺) to 6559 eV at 4.8 V (vs Li/Li⁺) in the first cycle. After full charging in the second cycle, the Mn K-edge peak remained at 6559 eV, indicating that Mn reached its highest oxidation state (Mn⁴⁺) at full charge during the first cycle. This confirms the complete oxidation of Mn during the initial charging process. The additional capacity observed between 4.5 and 4.8 V (Figure 2b) is likely due to the activation of the oxygen anion redox process, which occurs after Mn reaches its maximum oxidation state. This highlights the contribution of oxygen redox activity to the overall capacity at higher voltages.

At 25 °C, the Mn K-edge peak was observed at 6556 eV at 4.5 V (vs Li/Li⁺), which is 2 eV lower than at 60 °C, indicating a lower Mn oxidation state (Figure 10a). This suggests slower lithium delithiation and delayed activation of LRMO and the oxygen anion redox reaction, resulting in a lower charging capacity compared to that at 60 °C, as shown in Figure 2a,b. During charging at 25 °C, the Mn K-edge peak gradually shifted, reaching 6558 eV during the first cycle and 6559 eV after the second cycle (Figure 10b,c). This indicates that Mn was not fully oxidized during the first cycle but achieved complete oxidation by the second cycle. These observations are supported by the XRD data (Figure 9, Table S2, Supporting Information), which reveal fewer TM layer vacancies at 25 °C compared to at 60 °C. The reduced TM vacancy formation

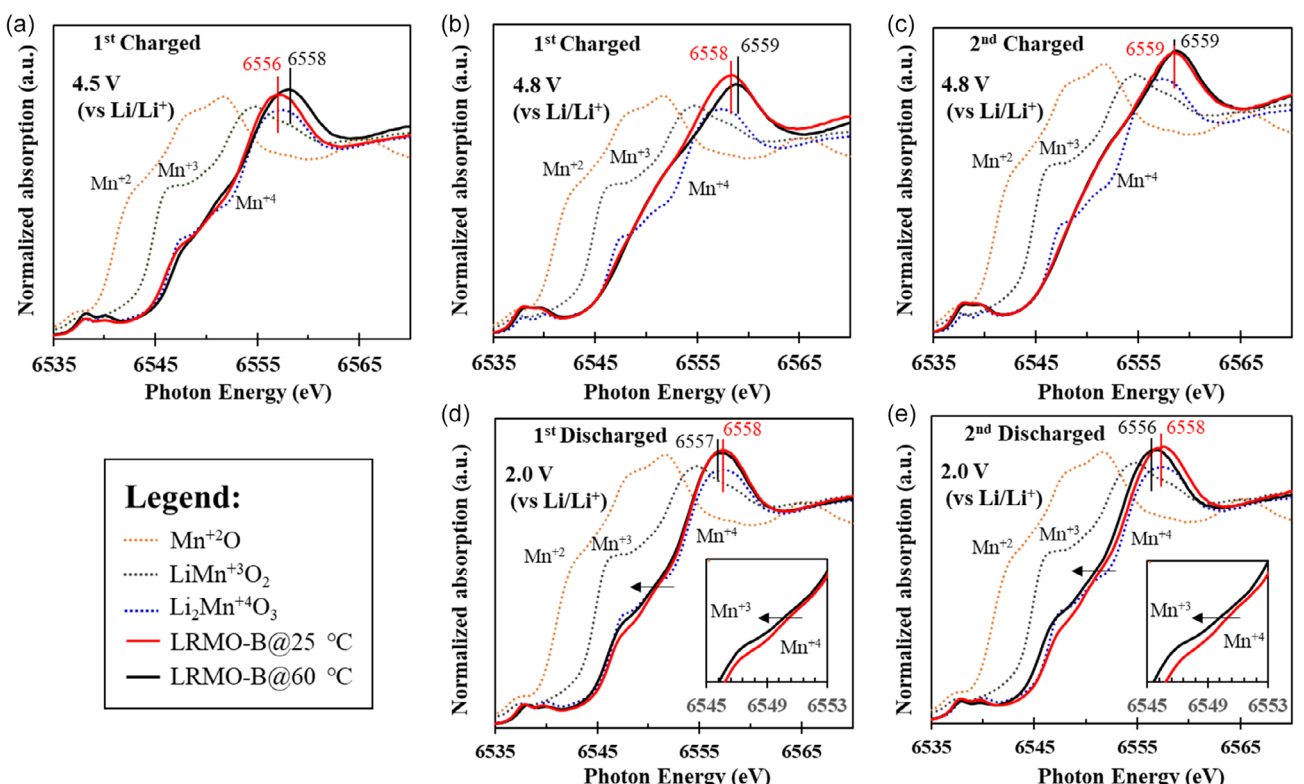


Figure 10. Mn K-edge XANES spectra for LRMO-B after a) the first and b) the second charge at 4.5 and 4.8 V, and c) after the second charge at 4.8 V. Corresponding discharge curves at 2.0 V for d) the first and e) the second discharge cycles. Reference spectra for Mn²⁺O, LiMn³⁺O₂, and Li₂Mn⁴⁺O₃ are included for comparison, providing insights into the oxidation states of Mn during cycling.

at 25 °C aligns with slower delithiation kinetics and delayed activation of the Li_2MnO_3 phase. These findings confirm that temperature plays a critical role in influencing the electrochemical performance and phase transitions of LRMO.

Figure 10d,e shows the Mn K-edge peak positions after discharging during the first and second cycles, respectively. At 25 °C, the Mn K-edge peak remained at 6558 eV after both the first and second discharges, indicating no significant change in Mn oxidation state. In contrast, at 60 °C, the Mn K-edge peak shifted to 6557 eV after the first discharge and further decreased to 6556 eV after the second discharge. Because lower energy peaks correspond to lower Mn oxidation states, as indicated by the reference samples in Figure 10, these results suggest that the activation of Li_2MnO_3 is more effective at higher temperatures. In contrast, the reduction in Mn oxidation state observed after the first and second discharges at 60 °C was not seen at 25 °C. This aligns with the lower capacity observed in Figure 2a and the absence of a Mn redox peak in the differential capacity curves (Figure 2c). In addition, the higher Mn oxidation state remaining after discharge at 25 °C suggests that a MnO_2 -like structure (Mn^{4+}) continues to dominate during charging and persists after discharging. This is consistent with the delayed lithiation observed during the discharge process at 25 °C.

The lower Mn oxidation state observed at 60 °C after discharging suggests that the crystal volume of the sample discharged at 25 °C should be smaller than that at 60 °C. This is because Mn^{4+} , with a smaller ionic radius (0.53 Å), occupies less space compared to Mn^{3+} (0.58 Å).^[51,52] This hypothesis is supported by Rietveld refinement results, which show that the unit cell volume of the sample discharged at 25 °C is 203 Å³, significantly smaller than the 207.23 Å³ observed at 60 °C (Table S2, Supporting Information).

Overall, the combined XRD and XANES results clearly show that temperature plays a vital role in the electrochemical behavior of LRMO by affecting its crystal structure and Mn oxidation state. Phase activation is significantly more pronounced at elevated temperatures, leading to notable changes in both the crystal structure and Mn oxidation state. At higher temperatures, faster delithiation and lithiation kinetics promote the formation of more TM layer vacancies at fully charged states and result in lower Mn oxidation states, which correspond to larger crystal volumes in the discharged state. In contrast, lower temperatures suppress these structural and electrochemical changes, delaying phase transitions and material activation. These findings highlight the critical influence of temperature on phase transformations, crystal structure evolution, and overall electrochemical performance in LRMO materials, underscoring its importance in optimizing their functionality.

2.7. Unlocking the Potential of LiNbO_3 -Coated LRMO at Room Temperature

To fully unlock the potential of LiNbO_3 -coated LRMO cathodes at 25 °C, it is essential to address the challenges of low electronic conductivity, increased cell resistance, and insufficient activation of the Li_2MnO_3 phase. To overcome these limitations, we propose

the addition of 2.5 wt% vapor-grown carbon fiber (VGCF), a carbon conductive additive that we have previously shown improves the electronic conductivity of cathode composites in ASSBs, reduces cell resistance, and enhances Li_2MnO_3 activation.^[29] This strategy aims to achieve capacities at 25 °C comparable to those currently observed at 60 °C.

The cycling performance of LRMO-Nb2 was evaluated within the voltage range of 2.0–4.8 V (vs Li/Li⁺) using a CC-constant potential (CC-CP) protocol (Figure 11a). At 25 °C, the CC rate was set to a current density of 150 μA cm⁻² (C/20 with a CP hold at C/200). At 60 °C, the CC rate was adjusted to a current density of 300 μA cm⁻² (C/10 with a CP hold at C/100). The charge-discharge profiles that were processed to exclude the CP hold data, retaining only the CC portions, are shown in Figure 11b.

The addition of VGCF significantly improved the electronic conductivity of the composite cathode, resulting in an initial capacity of 236.1 mAh g⁻¹ at C/20 (Figure 11a), compared to 200.7 mAh g⁻¹ at C/100 without VGCF (Figure 2a). This improvement highlights the critical role of increased conductivity in achieving higher initial capacities and optimizing cathode performance.^[31,32]

During CC-CP cycling at 25 °C (Figure 11a), the discharge capacity steadily increased until the 30th cycle, reaching a peak value of 340 mAh g⁻¹. It then remained stable, with only a slight decline to 337 mAh g⁻¹ by the 50th cycle. The CE consistently exceeded 99.5% after the first cycle, indicating excellent cycling stability. In CC-only mode, the initial capacity was 217.5 mAh g⁻¹,

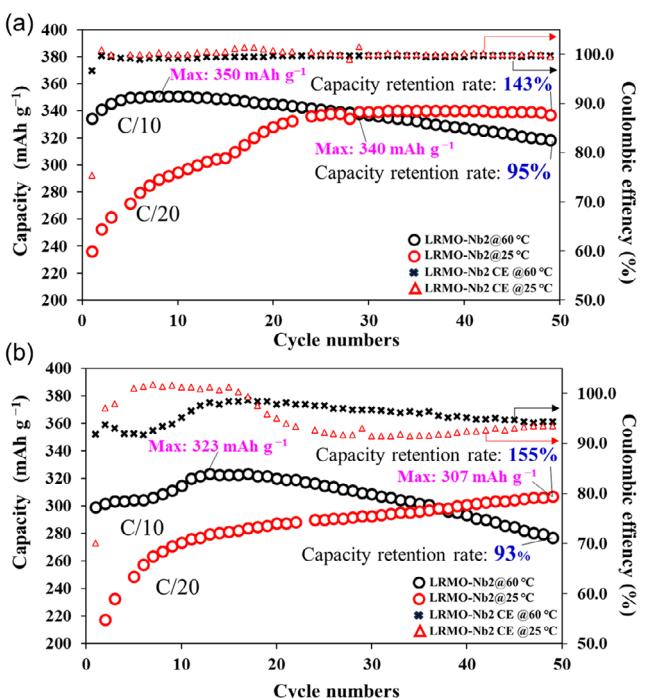


Figure 11. Cycling performance of LRMO-Nb2 evaluated over a voltage range of 2.0–4.8 V (vs Li/Li⁺) at 25 and 60 °C. a) Cycling results using a constant current-constant potential (CC-CP) protocol. At 25 °C, the CC rate was set to C/20, followed by a CP hold at C/200. At 60 °C, the CC rate was set to C/10, followed by a CP hold at C/100. b) Cycling results with charge-discharge profiles processed to exclude the CP hold data, showing only the CC portions.

which increased to 307 mAh g⁻¹ by the 50th cycle, resulting in a capacity retention rate of 155%. The increase in capacity retention rate can be attributed to the gradual activation of the Li₂MnO₃ phase during cycling. This activation process facilitates additional redox reactions, particularly involving oxygen anions, which significantly contribute to the observed capacity gains. Furthermore, improved conductivity plays a crucial role by reducing resistance and enabling more efficient charge transfer. This enhanced conductivity supports the progressive utilization of the active material, allowing for sustained capacity improvements over cycling. These findings demonstrate that improved conductivity not only reduces resistance but also enhances the phase activation of LRMO, resulting in significantly improved electrochemical performance at 25 °C.

At 60 °C, the reduced cell resistance enabled faster cycling rates. In CC-CP mode, the cell achieved a maximum capacity of 350 mAh g⁻¹ at C/10 by the fifth cycle, with capacity retention decreasing to 95% (318 mAh g⁻¹) after 50 cycles (Figure 11a). In CC-only mode, the cell reached a peak capacity of 324 mAh g⁻¹ by the 13th cycle, with capacity retention decreasing to 93% (277 mAh g⁻¹) after 50 cycles (Figure 11b). These findings demonstrate that elevated temperatures improve both electronic and ionic conductivity, leading to higher cell capacities. However, capacity degradation during extended cycling at 60 °C may be attributed to increased resistance caused by the degradation of the SE or structural deterioration of LRMO. This is supported by the observed current drop during CV measurements at elevated temperatures (Figure 5d). While higher temperatures enhance electrochemical performance by promoting faster kinetics and more efficient phase activation, they may also accelerate the long-term degradation of the SE or LRMO structure. To

confirm these mechanisms, further analyses such as XPS, TEM, and TOF-SIMS should be carried out to identify the degradation products in both the SE and LRMO.

Overall, the continuous increase in capacity observed at 25 °C suggests that not all electrochemically active sites are activated during the initial cycles, likely due to kinetic limitations under room-temperature conditions in the all-solid-state configuration. In contrast, at 60 °C, enhanced ionic and electronic conductivities facilitate the more complete activation of the Li₂MnO₃ component and the associated oxygen redox reactions, resulting in higher capacity and improved electrochemical performance after cycling. To validate the underlying mechanism of this phenomenon, the structural-electrochemical interplay of LRMO and its correlation with cycling performance at different temperatures is illustrated in Figure 12.

At 25 °C, the electrochemical behavior of LRMO indicates ongoing activation during CV measurements and reduced electronic conductivity during the initial charge-discharge process. XRD results reveal fewer TM vacancies and the presence of a MnO₂-like structure, with a higher average oxidation state (Mn⁴⁺) dominating the CAM after the initial discharge. These observations support the conclusion that the higher resistance of the ASSB cell at lower temperatures (Figure 4c) hinders the activation of LRMO. Since the electronic conductivity of LRMO can only be enhanced through full lithium intercalation during charge-discharge cycling (Figure 7)—when the Li₂MnO₃ phase transforms into LiMnO₂ (Equations (1)–(3))—the elevated resistance at low temperatures prevents complete lithium intercalation, thereby limiting the improvement in electronic conductivity. This also suggests that the LRMO particles are not fully activated at 25 °C, with a significant portion remaining in an unactivated state.

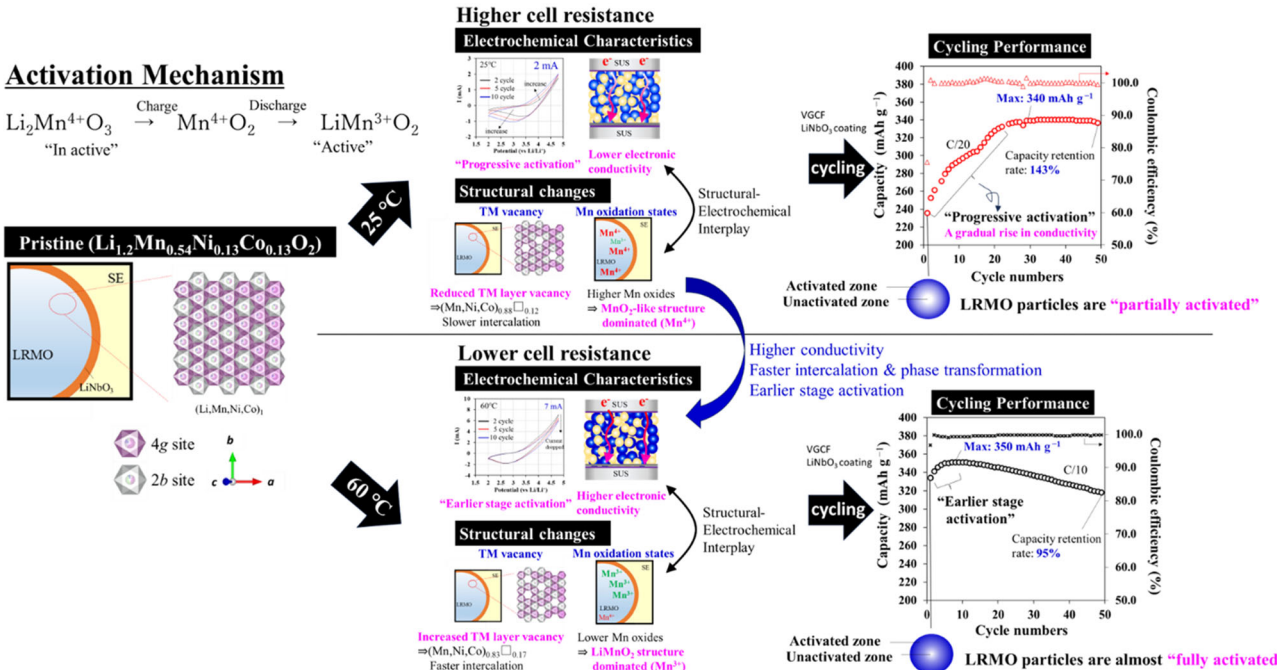


Figure 12. Schematic of the underlying mechanisms behind progressive activation at 25 °C and earlier-stage activation at 60 °C. The diagram highlights the structural-electrochemical interplay of LRMO and its correlation with cycling performance at different temperatures. SUS, stainless steel.

In contrast, at 60 °C, the cell resistance is sufficiently reduced to enable full lithium intercalation (Figure 4c), which promotes high Li-ion conductivity by facilitating transport through TM vacancies. This is supported by the observed increase in TM vacancy value and the lower average manganese oxidation state (Mn^{3+}) identified by XRD and XANES analyses (Figure 9 and 10). As a result, Li ions are smoothly de/intercalated into LRMO, leading to improved electronic conductivity and earlier-stage activation. This contributes to enhanced electrochemical performance, with only a small portion of the material remaining unactivated.

In conclusion, this study addresses the key challenges limiting the performance of LRMO cathodes at 25 °C and demonstrates significant improvements. By analyzing factors such as electronic conductivity and the activation of the Li_2MnO_3 phase, we identified the primary barriers to achieving high performance at low temperatures. Adding 2.5 wt% VGCF as a conductive additive effectively reduced cell resistance and enhanced phase activation, leading to significantly improved capacity and cycle stability. These results highlight that overcoming these challenges can optimize LRMO cathodes for ASSBs, providing a promising approach for developing high-performance ASSBs that operate efficiently at room temperature.

However, several challenges need to be addressed for further improvement. Future research should focus on optimizing the distribution of conductive additives to improve conductivity without compromising the cathode's structural integrity. In addition, the long-term stability and cycling performance of LRMO-based electrodes require further study, particularly concerning the degradation of the SE interphase and side reactions that may impact performance over extended cycles, especially at higher temperatures. Furthermore, enhancing the activation of the Li_2MnO_3 phase at lower temperatures is critical. Exploring advanced materials or coatings that improve lithium-ion diffusion will be essential for achieving better electrochemical performance at room temperature. These efforts will pave the way to achieving more efficient and durable LRMO-based cathodes in ASSBs.

3. Conclusion

This work presented a comprehensive assessment of the temperature-dependent electrochemical behavior of $LiNbO_3$ -coated LRMO cathodes in ASSBs. We demonstrated for the first time that phase activation of LRMO is the key factor in reducing resistance and enhancing performance at room temperature, surpassing the effects of elevated temperatures. Phase activation significantly improves electronic conductivity, lowers cell resistance, and optimizes charge transfer pathways. Unlike conductivity enhancements driven solely by higher temperatures, phase activation is shown to be essential for maximizing LRMO performance at both 25 and 60 °C. Specifically, phase activation boosts electronic conductivity by an eightfold increase at 25 °C and a tenfold increase at 60 °C, compared to a fivefold increase achieved through temperature elevation alone. These findings highlight the critical role of phase activation in enhancing the electrochemical performance of LRMO in

ASSBs, redefining its importance in achieving high efficiency at both room and elevated temperatures.

In addition, this study highlights the critical role of $LiNbO_3$ coatings in stabilizing the electrode–electrolyte interface, suppressing interfacial reactions, and reducing resistance. This stabilization improves conductivity and ensures stable performance, particularly at room temperature. By combining $LiNbO_3$ coatings with conductive additives, we presented an effective strategy to address the challenges of sluggish kinetics and high resistance at 25 °C. Our approach significantly reduces cell resistance, promotes phase activation, and achieves a high discharge capacity exceeding 300 $mAh\ g^{-1}$ after 30 cycles, demonstrating its potential for optimizing room-temperature performance in ASSBs.

Overall, this work tackles key challenges in improving room-temperature performance and structural stability, offering transformative insights for the development of advanced, high-energy-density LRMO-based cathodes. These findings lay a solid foundation for next-generation high-energy-density ASSBs and open new avenues for future innovations in solid-state energy storage systems.

4. Experimental Section

Materials and Characterization

All experimental procedures were conducted in an argon-filled glove box (dew point $<-80^\circ C$, oxygen concentration $<1\ ppm$). The materials used in this study included LRMO powder (GS Alliance Co., Ltd., Japan), argyrodite-type $Li_{(7-x)}PS_{(6-x)}Cl_x$ ($x \approx 1$, $\approx 1.8\ g\ cm^{-3}$, $\approx 2 \times 10^{-3}\ S\ cm^{-1}$, Mitsui Mining & Smelting, Japan) as the SE, and VGCF (Resonac Holdings Corporation, Japan) as the conductive additive. The In–Li alloy counter electrode was prepared by layering In foil (100 μm , Nilaco)/Li foil (200 μm , Honjo Metal)/In foil (300 μm).

A Li–Nb double alkoxide solution was used to form the $LiNbO_3$ -coated layer. The alkoxide was dissolved in anhydrous ethanol inside the glove box, following a previously published procedure.^[28–30] LRMO was then added to the solution and stirred for 1 h at room temperature. The solution was subsequently heated to 100 °C for 12 h, and the resulting gel was sintered at 300 °C for 3 h in oxygen to obtain the $LiNbO_3$ -coated layers in an amorphous state. Finally, the powder was baked at 120 °C in a vacuum oven for 12 h to evaporate any remaining water from the LRMO, to prevent it from reacting with the SE.

For material characterization and coated layer analysis, XRD measurements were conducted using a SmartLab XRD system (Rigaku) with Mo K α radiation. The uniformity and morphology of the coated layers were analyzed using a field-emission SEM (JSM-7900F, JEOL), equipped with an EDX detector (Ultim Max, Oxford Instruments) at an accelerating voltage of 15 kV. The relationship between the amount of $LiNbO_3$ on the surface of LRMO and the calculated $LiNbO_3$ fraction was investigated using ICP-MS (Agilent 7700x). The thickness of the $LiNbO_3$ -coated layers was measured using high-resolution transmission electron microscopy (TEM; JEM-ARM200F, JEOL). Structural and chemical changes were further analyzed through Rietveld refinement using Rietveld analysis program for Windows-full pattern-FP for XRD data and XANES analysis of the Mn K-edge. The XANES measurements were performed at a synchrotron radiation facility (AichiSR) using the hard X-ray XAFS Beamline (BL5S1) to track the oxidation state evolution of manganese in both the fully charged and discharged states. The refined crystal structures were visualized using VESTA.^[31,32]

Cell Assembly

The ASSB cells were assembled in a bulk-type configuration. Bare LRMO (LRMO-B) and LiNbO₃-coated LRMO particles with concentrations of 0.2 wt% (LRMO-Nb1), 0.5 wt% (LRMO-Nb2), 1.8 wt% (LRMO-Nb3), and 3.2 wt% (LRMO-Nb4) were manually mixed with the SE at a weight ratio of 7:3 in an agate mortar for 10 min to prepare the composite positive electrode. A separator pellet was formed by pressing 127.3 mg of the SE at 98 MPa in a ceramic cylinder with a cross-sectional area of 1 cm². The cathode mixture (16.4 mg) was then uniformly spread onto one side of the separator layer and pressed together with the SE separator at 588 MPa. The reversible capacity of LRMO, based on its performance in liquid lithium-ion battery systems ($\approx 265 \text{ mAh g}^{-1}$), was used to calculate the areal capacity of the ASSB cells in this study. A total of 11.33 mg of active material was applied over an electrode area of 1 cm², resulting in an areal mass loading of 11.33 mg cm⁻². Based on this calculation, the corresponding areal capacity was 3.00 mAh cm⁻². The In-Li alloy was pressed onto the opposite side of the separator layer at 98 MPa to provide a stable anode potential of 0.62 V (vs Li/Li⁺). The sandwiched pellet cell was held between two stainless steel (SUS) rods, which acted as current collectors for the positive and negative electrodes. The cell was secured horizontally with three bolts and placed in a gas-sealed container for electrochemical measurements under a pressure of 200 MPa, as outlined in a previously published procedure.^[29,30]

For the initial capacity test, cells were charged and discharged for three cycles within the voltage range of 2.0–4.8 V (vs Li/Li⁺) at a CC density of 30 $\mu\text{A cm}^{-2}$ (C/100), without the addition of a carbon conductive additive. The cells were held at a constant voltage with a cutoff current of 3 $\mu\text{A cm}^{-2}$ (C/1000) at 25 °C. This low rate was selected to fully utilize the potential of the particles. The tests were performed using a charge-discharge measuring device (580, Scribner) in a thermostatic chamber (SU-222, Espec). AC impedance measurements were conducted with an impedance analyzer (VSP-300, Biologic) in the frequency range from 10⁻² to 10⁶ Hz, with an applied voltage of 10 mV for all cells after three cycles.

To investigate the effect of electronic conductivity on electrochemical behavior, VGCF was incorporated into both LRMO-B and -Nb2 at a weight ratio of LRMO:SE:VGCF = 7.0:2.75:0.25. The VGCF-added cells were cycled for 50 cycles within the voltage range of 2.0–4.8 V (vs Li/Li⁺) at a CC density of 150 $\mu\text{A cm}^{-2}$ (C/20), followed by a CP hold with a cutoff current of 15 $\mu\text{A cm}^{-2}$ (C/200) at 25 °C. In addition, the cells were tested under a CC density of 300 $\mu\text{A cm}^{-2}$ (C/10) with a CP hold and a cutoff current of 30 $\mu\text{A cm}^{-2}$ (C/100) at 60 °C. All tests were conducted using a charge-discharge measuring device (580, Scribner) in a thermostatic chamber (SU-222, Espec).

Direct Current and CV Measurements

DC measurements were performed using a cell setup that featured a reversible Li-In alloy anode and an ion-blocking inert electrode (SUS foil) at 25 and 60 °C. The electronic properties of the LRMO-B sample were investigated with and without the SE mixture using Hebb-Wagner measurements^[45–47] and a multichannel potentiostat (VSP-300, Biologic). For the cell setup, LRMO-B particles and the SE were mixed at a weight ratio of 7:3 in an agate mortar. A 100 mg portion of the mixture was pressed into a pellet with a 1 cm² area at 588 MPa. The In-Li alloy was then pressed onto the opposite side of the separator at 98 MPa to establish a stable anode potential of 0.62 V (vs Li/Li⁺). The pellet was sandwiched between two SUS plates acting as current collectors, with SUS foil placed beneath the SS plates as the inert electrode. The pelletized cells were secured horizontally using three bolts and placed in an airtight container.

For CV measurements, the same cell setup was used for 10 cycles between 2.0 and 4.8 V (vs Li/Li⁺) at a sweep rate of 1.0 mV s⁻¹. The cell resistance was measured before and after the DC and CV

measurements using AC impedance spectroscopy. The measurements were conducted at 25 and 60 °C with an impedance analyzer (VSP-300, Biologic) in the frequency range from 10⁻² to 10⁶ Hz, with an applied voltage of 10 mV. The results were analyzed to determine the resistances associated with electronic conduction in the composite cathode material, comparing the LRMO-B sample with and without SE.

Acknowledgements

This study was supported by the SOLID-Next project (grant no. JPNP23005) commissioned by the New Energy and Industrial Technology Development Organization (NEDO).

Conflict of Interest

The authors declare no conflict of interest.

Author Contributions

Willy Shun Kai Bong: data curation (lead); formal analysis (lead); investigation (lead); methodology (lead); visualization (lead); writing—original draft (lead); and writing—review and editing (lead). **Naoya Ishida:** data curation (supporting); investigation (supporting); methodology (supporting); and writing—review and editing (supporting). **Shoko Kitabayashi:** investigation (supporting). **Masaki Shimada:** methodology (supporting). **Koji Kawamoto:** supervision (lead). **Takuhiro Miyuki:** project administration (lead). **Minoru Kuzuhara:** supervision (lead).

Data Availability Statement

The data that support the findings of this study are available from the corresponding author upon reasonable request.

Keywords: all-solid-state batteries · electronic conductivities · LiNbO₃ coatings · Li-rich Mn-based oxides · phase activation

- [1] J.-M. Tarascon, M. Armand, *Nature* **2001**, *414*, 359.
- [2] R. Weber, M. Genovese, A. J. Louli, S. Hames, C. Martin, I. G. Hill, J. R. Dahn, *Nat. Energy* **2019**, *4*, 683.
- [3] M. M. Thackeray, C. Wolverton, E. D. Isaacs, *Energy Environ. Sci.* **2012**, *5*, 7854.
- [4] Y. Kato, S. Hori, T. Saito, K. Suzuki, M. Hirayama, A. Mitsui, M. Yonemura, H. Iba, R. Kanno, *Nat. Energy* **2016**, *1*, 16030.
- [5] W. Lee, S. Muhammad, C. Sergey, H. Lee, J. Yoon, Y.-M. Kang, W.-S. Yoon, *Angew. Chem. Int. Ed.* **2020**, *59*, 2578.
- [6] J. Zheng, S. Myeong, W. Cho, P. Yan, J. Xiao, C. Wang, J. Cho, J.-G. Zhang, *Adv. Energy Mater.* **2017**, *7*, 1601284.
- [7] W. He, W. Guo, H. Wu, L. Lin, Q. Liu, X. Han, Q. Xie, P. Liu, H. Zheng, L. Wang, X. Yu, D.-L. Peng, *Adv. Mater.* **2021**, *33*, 2005937.
- [8] H. Gao, S. Xin, L. Xue, J. B. Goodenough, *Chem* **2018**, *4*, 833.
- [9] Y. Han, S. H. Jung, H. Kwak, S. Jun, H. H. Kwak, J. H. Lee, S. T. Hong, Y. S. Jung, *Adv. Energy Mater.* **2021**, *11*, 2100126.
- [10] W. Du, Q. Shao, Y. Wei, C. Yan, P. Gao, Y. Lin, Y. Jiang, Y. Liu, X. Yu, M. Gao, W. Sun, H. Pan, *ACS Energy Lett.* **2022**, *7*, 3006.
- [11] K. Hikima, K. Suzuki, S. Taminato, M. Hirayama, S. Yasuno, R. Kanno, *Chem. Lett.* **2019**, *48*, 192.

- [12] X. Yin, D. Li, L. Hao, Y. Wang, Y. Wang, X. Guo, S. Zhao, B. Wang, L. Wu, H. Yu, *Chem. Commun.* **2023**, *59*, 639.
- [13] B. Chen, J. Zhang, D. Wong, T. Wang, T. Li, C. Liu, L. Sun, X. Liu, *Angew. Chem. Int. Ed.* **2024**, *63*, e202315856.
- [14] Y. Wang, D. Wu, P. Chen, P. Lu, X. Wang, L. Chen, H. Li, F. Wu, *Adv. Funct. Mater.* **2023**, *34*, 2309822.
- [15] Z. Wu, Q. Shao, Y. Wei, C. Yan, P. Gao, Y. Lin, Y. Jiang, Y. Yang, J. Chen, Y. Liu, M. Gao, W. Sun, H. Pan, *Nano Energy* **2024**, *122*, 109281.
- [16] N. Hu, Y.-H. Zhang, Y. Yang, H. Wu, Y. Liu, C. Hao, Y. Zheng, D. Sun, W. Li, J. Li, Z. Hu, T.-S. Chan, C.-W. Kao, Q. Kong, X. Wang, S.-C. Haw, J. Ma, G. Cui, *Adv. Energy Mater.* **2024**, *14*, 2303797.
- [17] S. Sun, C.-Z. Zhao, H. Yuan, Z.-H. Fu, X. Chen, Y. Lu, Y.-F. Li, J.-K. Hu, J. Dong, J.-Q. Huang, M. Ouyang, Q. Zhang, *Sci. Adv.* **2022**, *8*, eadd5189.
- [18] R. Yu, C. Wang, H. Duan, M. Jiang, A. Zhang, A. Fraser, J. Zuo, Y. Wu, Y. Sun, Y. Zhao, J. Liang, J. Fu, S. Deng, Z. Ren, G. Li, H. Huang, R. Li, N. Chen, J. Wang, X. Li, C. V. Singh, X. Sun, *Adv. Mater.* **2023**, *35*, 2207234.
- [19] A. Zhang, J. Wang, R. Yu, H. Zhuo, C. Wang, Z. Ren, J. Wang, *ACS Appl. Mater. Interfaces* **2023**, *15*, 8190.
- [20] D. Cao, Y. Zhang, A. M. Nolan, X. Sun, C. Liu, J. Sheng, Y. Mo, Y. Wang, H. Zhu, *Nano Lett.* **2020**, *20*, 14833.
- [21] Y. Li, D. Zhang, X. Xu, Z. Wang, Z. Liu, J. Shen, J. Liu, M. Zhu, *J. Energy Chem.* **2021**, *60*, 32.
- [22] X. Li, Q. Ye, Z. Wu, W. Zhang, H. Huang, Y. Xia, Y. Gan, X. He, X. Xia, J. Zhang, *Electrochim. Acta* **2023**, *453*, 142361.
- [23] W. E. Gent, K. Lim, Y. Liang, Q. Li, T. Barnes, S.-J. Ahn, K. H. Stone, M. McIntire, J. Hong, J. H. Song, Y. Li, A. Mehta, S. Ermon, T. Tyliszczak, D. Kilcoyne, D. Vine, J.-H. Park, S.-K. Doo, M. F. Toney, W. Yang, D. Prendergast, W. C. Chueh, *Nat. Commun.* **2017**, *8*, 2091.
- [24] G. Song, S. Lee, T. Kim, M. S. Jung, K. Kim, S. H. Choi, S. Lee, J. Park, M. Lee, C. Park, M.-S. Kwon, K. T. Lee, *Adv. Energy Mater.* **2024**, *14*, 2403374.
- [25] T. Ohzuku, M. Nagayama, K. Tsuji, K. Ariyoshi, *J. Mater. Chem.* **2011**, *21*, 10179.
- [26] F. A. Susai, M. Talianker, J. Liu, T. Rosy, *Materials* **2020**, *13*, 4388.
- [27] A. Ito, D. Li, Y. Ohsawa, Y. Sato, *J. Power Sources* **2008**, *183*, 344.
- [28] N. Ohta, K. Takada, I. Sakaguchi, L. Zhang, R. Ma, K. Fukuda, M. Osada, T. Sasaki, *Electrochem. Commun.* **2007**, *9*, 1486.
- [29] W. S. K. Bong, K. Kawamoto, *ECS Adv.* **2024**, *3*, 020503.
- [30] W. S. K. Bong, A. Shiota, T. Miwa, Y. Morino, S. Kanada, K. Kawamoto, *J. Power Sources* **2023**, *577*, 233259.
- [31] K. Momma, F. Izumi, *J. Appl. Cryst.* **2011**, *44*, 1272.
- [32] K. Momma, F. Izumi, *J. Appl. Cryst.* **2008**, *41*, 653.
- [33] N. Ishida, N. Tamura, N. Kitamura, Y. Idemoto, *J. Power Sources* **2016**, *319*, 255.
- [34] Y. Idemoto, R. Kawai, N. Ishida, N. Kitamura, *J. Power Sources* **2015**, *273*, 1023.
- [35] D. Zuo, G. Tian, X. Li, D. Chen, K. Shu, *J. Alloy. Compd.* **2017**, *706*, 24.
- [36] X. Li, Q. Sun, Z. Wang, D. Song, H. Zhang, X. Shi, C. Li, L. Zhang, L. Zhu, *J. Power Sources* **2020**, *456*, 227997.
- [37] Y. Morino, *J. Power Sources* **2022**, *541*, 231672.
- [38] S. Hu, A. S. Pillai, G. Liang, W. K. Pang, H. Wang, Q. Li, Z. Guo, *Electrochem. Energy Rev.* **2019**, *2*, 277.
- [39] M. M. Thackeray, S.-H. Kang, C. S. Johnson, J. T. Vaughan, R. Benedek, S. A. Hackney, *J. Mater. Chem.* **2007**, *17*, 3112.
- [40] J.-Y. Luo, Y.-G. Wang, H.-M. Xiong, Y.-Y. Xia, *Chem. Mater.* **2007**, *19*, 4791.
- [41] S. J. Shi, J. P. Tu, Y. Y. Tang, Y. Q. Zhang, X. L. Wang, C. D. Gu, *J. Power Sources* **2013**, *240*, 140.
- [42] J. R. Croy, D. Kim, M. Balasubramanian, K. Gallagher, S.-H. Kang, M. M. Thackeray, *J. Electrochem. Soc.* **2012**, *159*, A781.
- [43] B. Liu, N. Hu, C. Li, J. Ma, J. Zhang, Y. Yang, D. Sun, B. Yin, G. Cui, *Angew. Chem. Int. Ed.* **2022**, *61*, e202209626.
- [44] S. Kaewmala, W. Limphirat, V. Yordsri, H. Kim, S. Muhammad, W.-S. Yoon, S. Sriolomsak, P. Limthongkul, N. Meethong, *Sci. Rep.* **2019**, *9*, 427.
- [45] J. R. Macdonald, in *Impedance Spectroscopy, Emphasizing Solid Materials and Systems*, John Wiley & Sons, Inc., New York, NY **1987**.
- [46] C. Wagner, in *Presented at the Proc. of 7th Meeting CITCE*, Lindau **1995**.
- [47] B. J. Neudecker, W. Weppner, *J. Electrochem. Soc.* **1996**, *143*, 2198.
- [48] Z. Xi, Q. Sun, J. Li, Y. Qiao, G. Min, L. Ci, *Molecules* **2024**, *29*, 1064.
- [49] X. He, J. Wu, Z. Zhu, H. Liu, N. Li, D. Zhou, X. Hou, J. Wang, H. Zhang, D. Bresser, Y. Fu, M. J. Crafton, B. D. McCloskey, Y. Chen, K. An, P. Liu, A. Jain, J. Li, W. Yang, Y. Yang, M. Winter, R. Kostecki, *Energy Environ. Sci.* **2022**, *15*, 4137.
- [50] H. Chen, M. S. Islam, *Chem. Mater.* **2016**, *28*, 6656.
- [51] M. R. A. Kishore, H. Okamoto, L. Patra, R. Vidya, A. O. Sjästad, H. Fjellvåg, P. Ravindran, *Phys. Chem. Chem. Phys.* **2016**, *18*, 27885.
- [52] M. Gao, Y. Pan, Y. Jin, J. Lin, *RSC Adv.* **2021**, *11*, 760.

Manuscript received: January 26, 2025

Revised manuscript received: April 7, 2025

Version of record online: April 19, 2025